Transient response of offshore wind turbines on monopiles in sand
Role of cyclic hydro-mechanical soil behaviour

Corciulo, Simone; Zanoli, Omar; Pisanò, Federico

Publication date
2017

Document Version
Accepted author manuscript

Published in
Computers and Geotechnics

Citation (APA)
Corciulo, S., Zanoli, O., & Pisanò, F. (2017). Transient response of offshore wind turbines on monopiles in sand: Role of cyclic hydro-mechanical soil behaviour. *Computers and Geotechnics*, *83*, 221-238.

Postprint of Computers and Geotechnics
Volume 83, March 2017, Pages 221–238
Link to formal publication (Elsevier): http://dx.doi.org/10.1016/j.compgeo.2016.11.010

Transient response of offshore wind turbines on monopiles in sand: role of cyclic hydro–mechanical soil behaviour

Simone Corciulo
D'Appolonia S.p.A. – Marine & Offshore Engineering
Via Martiri di Cefalonia 2, 20097, San Donato Milanese, Italy

Omar Zanoli
D'Appolonia S.p.A. – Marine & Offshore Engineering
Via Martiri di Cefalonia 2, 20097, San Donato Milanese, Italy

Federico Pisanò
Geo-Engineering Section/Offshore Engineering Section
Faculty of Civil Engineering and Geoscience
Delft University of Technology
Stevinweg 1, 2628 CN Delft, The Netherlands
(corresponding author – e-mail: F.Pisano@tudelft.nl)

Abstract

Offshore wind turbines (OWTs) in relatively shallow waters are most often founded on monopile foundations, whose design is extremely relevant to the OWT dynamic performance under environmental loading.

In this study, 3D finite element (FE) modelling is applied to the dynamic analysis of OWTs and proposed as a valuable support to current design practice. FE results are presented about the interplay of cyclic soil behaviour and hydro-mechanical coupling in determining the OWT natural frequency: in dilative sands, the natural frequency seems not to decrease monotonically at increasing loading amplitude, while slight influence of soil permeability is found.

Keywords: offshore wind turbine, monopile, sand, Finite Element Method, cyclic modelling, hydro-mechanical coupling, dynamic analysis

1 Introduction

The gradual depletion of hydrocarbon reserves is currently pushing the energy market towards clean and sustainable sources, with solar and wind energies expected to play a major role in the coming decades. In this context, several European countries have been recently investing on the installation of offshore wind turbines (OWTs). According to the European Wind Energy Association (EWEA), Europe currently leads the offshore wind industry with a total offshore power capacity of 8 GW in 2014, to become 24 GW by 2020 and 66.5 GW by 2030 (Gazzo et al., 2015).

At present, most OWTs in Europe are supported by monopile foundations (Arapogianni et al., 2013), open-ended steel tubes driven into the seabed by means of hydraulic hammers (Doherty and Gavin, 2012). Large monopiles having 4–6 m diameter are routinely employed in relatively shallow waters (up to 30 m), while diameters close to 10 m are currently being considered for bigger 6–7 MW OWTs in water depths up to 60 m (Doherty and Gavin, 2012). Monopile design is closely related to OWT dynamics, and in particular to the natural frequency f_0 associated with the first cantilever-like eigenmode. To avoid undesired resonance, OWTs are usually designed to keep f_0 within the $f_{1P} - f_{3P}$ range, where f_{1P} ($= 0.15 \div 0.25$ Hz) is the rotor revolution frequency, while f_{3P} ($= 3f_{1P} = 0.45 \div 0.75$ Hz for three-bladed OWTs) denotes the frequency of the aerodynamic pulses induced by the passage of the blades (*shadowing effect*). Setting $f_{1P} < f_0 < f_{3P}$ is commonly referred to as "soft–stiff" design, as it combines a stiff superstructure with a compliant (thus less expensive) foundation (Kühn, 2001; van der Tempel, 2006; Bhattacharya et al., 2013; Damgaard et al., 2014; Kallehave et al., 2015). Profound understanding of dynamic soil–monopile interaction is therefore needed for an accurate evaluation of f_0.

In light of these premises, numerous research programmes have been recently carried out to improve the prediction of (i) soil–monopile lateral stiffness (Cuéllar, 2011; Kallehave et al., 2012; Bhattacharya et al., 2013; Lombardi et al., 2013; Damgaard et al., 2014; Thieken et al., 2015a,b; Byrne et al., 2015a; Zdravković et al., 2015; Byrne et al., 2015b; Arany et al., 2016; Versteijlen et al., 2016) and (ii) the displacements/rotations accumulated after thousands of loading cycles (Achmus et al., 2009; LeBlanc et al., 2010; Bienen et al., 2011; Rudolph et al., 2014).

This paper targets a contribution to monopile design based on the modern feasibility of 3D finite element (FE) simulations, in agreement with the recent research agenda of the European Academy of Wind Energy (EAWE) (van Kuik et al., 2016): "*what is the amount of soil damping for an offshore turbine? Is it possible to estimate soil damping from first principles, like from numerical simulation with solid elements?*" Despite the quite generic terminology, the EAWE agenda points out the relevance of dissipative phenomena (*damping*) and their 3D numerical simulation (via *solid elements*). Some of these issues have been previously addressed in the field of geotechnical earthquake engineering (Kramer, 1996; Zienkiewicz et al., 1999), such as the contemporary presence of (slow) dynamics, cyclic soil response and hydro-mechanical (HM) coupling. It seems thus sensible to reorient this existing knowledge towards OWT applications, as recently attempted by Cuéllar et al. (2014).

The same modelling philosophy of Cuéllar et al. (2014) is here extended to the integrated analysis of soil–monopile–OWT systems under environmental loading (wind and waves). In particular, the transient response of a standard 5 MW OWT is simulated to illustrate, under different loading scenarios, the interplay of cyclic loading and HM effects in determining f_0. The ultimate goal is to promote dynamic 3D HM FE calculations as a support to geotechnical design in offshore wind applications. It is shown that more advanced FE modelling may unravel important geotechnical aspects, possibly not emerging from standard analysis.

2 3D FE modelling of soil–monopile–OWT systems

This section describes the main features of the soil–monopile–OWT FE model and refers to the most relevant background literature. The FE model has been set up through the OpenSees simulation platform (`http://opensees.berkeley.edu`, McKenna (1997); Mazzoni et al. (2007)), while the GID software (Melendo et al., 2015) has been employed to post-process all numerical results. It is shown that soil–monopile interaction in OWTs can be naturally investigated within the same modelling framework already applied to seismically loaded piles (Elgamal et al., 2009; Elgamal and Lu, 2009; Cheng and Jeremić, 2009; Lu et al., 2011).

2.1 Dynamic analysis of water-saturated soils

Governing equations Based on the work by Zienkiewicz and coworkers (Zienkiewicz et al., 1980; Zienkiewicz and Shiomi, 1984; Zienkiewicz et al., 1999), the so-called *u–p* formulation is here adopted to describe the dynamic HM response of the soil around the monopile. The *u–p* approach relies upon the assumption of negligible soil-fluid relative acceleration (Zienkiewicz et al., 1980; López-Querol et al., 2008), which seems appropriate for offshore wind applications (wind/wave loading frequencies are normally lower than 0.5 Hz – see Sections 2.3 and 4.1).

FE solution The *u-p* formulation leads to the following discrete system (Zienkiewicz and Shiomi, 1984; Jeremić et al., 2008):

$$\text{mixture equilibrium:} \quad \overbrace{\mathbf{M}\ddot{\mathbf{d}}}^{\text{mixture inertiae}} + \overbrace{\int_\Omega \mathbf{B}^T \boldsymbol{\sigma}' d\Omega}^{\text{soil internal forces}} - \overbrace{\mathbf{Q}\mathbf{p}}^{\text{pore pressure forces}} = \overbrace{\mathbf{f}^{ext}_{u,\Omega} + \mathbf{f}^{ext}_{u,\Gamma}}^{\text{mixture external forces}} \tag{1a}$$

$$\text{water mass balance:} \quad \overbrace{\mathbf{Q}^T\dot{\mathbf{d}}}^{\text{soil dilation/compaction}} + \overbrace{\mathbf{S}\dot{\mathbf{p}}}^{\text{fluid compressibility}} + \overbrace{\mathbf{H}\mathbf{p}}^{\text{seepage}} = \overbrace{\mathbf{f}^{ext}_{p,\Gamma} + \mathbf{f}^{ext}_{p,\Omega}}^{\text{fluid external fluxes}} \tag{1b}$$

based on the standard approximations $\mathbf{u} \approx \mathbf{N}_u\mathbf{d}$ and $p \approx \mathbf{N}_p\mathbf{p}$ for the displacement and the pore pressure fields, respectively (dots stand for time derivatives). If the interpolation functions in the arrays $\mathbf{N}_u$ and $\mathbf{N}_p$ do not fulfil the so-called *inf–sup* condition (Babuška, 1973; Brezzi, 1974), then spurious pore pressure oscillations ("checkerboard" modes) may arise as the the undrained-incompressible limit is approached (Zienkiewicz et al., 1999; Preisig and Prévost, 2011; McGann et al., 2012, 2015). This inconvenience is avoided here by resorting to the H1-P1ssp stabilised element formulation, recently proposed by McGann et al. (2015) and applied for the first time to 3D OWT problems. Despite the low/equal order formulation, eight-node H1-P1ssp brick elements prove suitable against pressure oscillation owing to a non-residual–based stabilization (Huang et al., 2004), producing an additional laplacian term in Equation (1b) (McGann et al., 2015):

$$\mathbf{Q}^T\dot{\mathbf{d}} + \left(\mathbf{S} + \tilde{\mathbf{H}}\right)\dot{\mathbf{p}} + \mathbf{H}\mathbf{p} = \mathbf{f}^{ext}_{p,\Gamma} + \mathbf{f}^{ext}_{p,\Omega}, \quad \text{where:} \quad \tilde{\mathbf{H}} = \bigwedge_{m=1}^{N_{el}} \left(\int_{\Omega^e} \boldsymbol{\nabla}\mathbf{N}_p^T \alpha \boldsymbol{\nabla}\mathbf{N}_p d\Omega^e \right) \tag{2}$$

and preventing the well-known numerical issues associated with vanishing compressibility and permeability matrices ($\mathbf{S}$ and $\mathbf{H}$ in (1)). On the practical side, the value of the α coefficient in (2) governs the "amount of stabilisation" injected into system (1)[1]. In what follows, the suggestion by McGann et al. (2015) is taken as a reference:

$$\alpha = \frac{\alpha_0 h_{el}^2}{G_s + \frac{4}{3}K_s} \tag{3}$$

[1]Too low or high α will result in either ineffective or excessive stabilisation. Excessive stabilisation means an unrealistic/unphysical attenuation of the pore pressure field, due to the diffusive nature of the stabilising term (2).

where h_{el} is, heuristically, the average element size within the FE mesh, G_s and K_s are the bulk and shear moduli of the soil skeleton, whilst α_0 is a scalar coefficient in the range of 0.1–0.5.

As for time integration, the well-known Newmark integration method is employed with parameters $\beta = 0.6$ and $\gamma = (\beta + 1/2)^2/4 = 0.3025$ (Hughes, 1987). Soil constitutive equations are integrated at Gauss points via the explicit forward Euler algorithm (Sloan, 1987).

Cyclic sand modelling The numerical analysis of environmentally loaded OWTs is strictly connected to the modelling of cyclic soil behaviour[2]. The present study relies upon the multi-surface plasticity model by Yang and Elgamal (2008) (UCSD08 model), featuring: (i) non-linear hypoelastic law; (ii) frictional shear strength criterion with non-circular deviatoric π–section (Lade and Duncan, 1975); (iii) non-linear shear stress–strain response generated by multiple nested yield surfaces (Mróz et al., 1978; Prévost, 1985); (iv) phase transformation line to distinguish dilative and compactive responses (Ishihara et al., 1975); (v) ability to reproduce both liquefaction and cyclic mobility during undrained loading (Yang et al., 2003; Elgamal et al., 2003). The interested reader is referred to Yang et al. (2003); Elgamal et al. (2003); Yang and Elgamal (2008) for details on the model formulation and the calibration of constitutive parameters.

Unlike other cyclic models (see e.g. Dafalias and Manzari (2004)), the UCSD08 formulation is not sensitive to variations in void ratio and cannot reproduce sand densification around the monopile (LeBlanc et al., 2010; Bhattacharya et al., 2013). However, densification effects are not deemed too relevant when the transient OWT response is analysed over relatively short loading events.

2.2 Monopile and superstructure

Elongated hollow structures may be idealised as general three-dimensional solids, cylindrical shells or beams. In this work, the superstructure (wind tower and transition piece) is modelled as a Timoshenko beam to account for combined bending and shear deformations (De Borst et al., 2012); conversely, the monopile is represented as a tubular 3D solid to reproduce genuine 3D effects in soil-structure interaction. In the same respect, one-phase 3D ssp bricks are preferred over shell elements for easier pre/post-processing procedures, especially when different solid formulations (one-phase and two-phase) coexist within the same OpenSees FE model. From the kinematic standpoint, the "mixed" structure formed by the 3D monopile and the OWT beam responds as a single Timoshenko beam, as long as rigid translational links are set between the OWT base and the monopile head.

Linear elastic behaviour is assumed for the whole steel structure, while 5% Rayleigh damping is set at 0.2 Hz and 8 Hz to generate low-frequency energy dissipation (Chopra, 1995).

2.3 Wind and wave loading

This section describes a simplified approach to create plausible wind/wave loading scenarios by assuming that: (i) wind and wave thrust forces on the OWT, F_{wind} and F_{wave}, depend mainly on the wind speed, the OWT geometry and certain empirical aero/hydro-dynamic factors; (ii) F_{wind} and F_{wave} are co-directional; (iii) the effect of rotor revolution on the wind speed around the OWT is negligible.

F_{wind} is evaluated through the so-called Blade Element Momentum (BEM) theory (Moriarty and Hansen, 2005; Lanzafame and Messina, 2007; Manwell et al., 2010; Madsen et al., 2010; Masters et al., 2014), regarding the rotor as a permeable actuator disc removing energy from a stream–tube-like wind flow. Simple considerations on fluid momentum and energy balance lead

[2]Reviews of the cyclic soil models proposed in the last decades are provided, for instance, by Prévost and Popescu (1996); Zienkiewicz et al. (1999); di Prisco and Wood (2012); Pisanò and Jeremić (2014).

to the following wind thrust formula:

$$F_{wind}(t) = \frac{1}{2} A_{disc} C_T \rho_{air} V_{wind}^2(t) \tag{4}$$

where t is time, A_{disc} the area of the disc/rotor, $\rho_{air} = 1.2\,\mathrm{kg/m^3}$ the air density and $C_T = 0.688$ is an empirical wind thrust coefficient.

As for wave loading, F_{wave} is determined through the simplifying assumption of *fully developed sea*. Accordingly, the existence of an equilibrium sea state under a steady wind field is postulated, so that a wave power spectrum can be employed to quantify the wave energy S associated with each oscillation frequency f (Pierson and Moskowitz, 1964; Hasselmann et al., 1973; Ochi and Hubble, 1976; Huang et al., 1981). The single-parameter spectral formulation by Pierson and Moskowitz (PM spectrum) is adopted (Pierson and Moskowitz, 1964):

$$S_{PM}(f) = \frac{\alpha g^2}{(2\pi f)^5} \exp\left[-\beta \left(\frac{g}{2\pi f V_{wind}^{19.5\mathrm{m}}}\right)^4\right] \tag{5}$$

where $\alpha = 0.0081$ and $\beta = 0.74$ are two dimensionless empirical factors, g the gravity acceleration and $V_{wind}^{19.5m}$ the wind speed at 19.5 m above sea surface[3]. The wave frequency f_S at the maximum spectral amplitude and the corresponding wave height H_S can be easily derived as:

$$f_S^4 = \frac{4\beta}{5}\left(\frac{g}{2\pi V_{wind}^{19.5\mathrm{m}}}\right)^4 \qquad H_S = 2\sqrt{\frac{\alpha}{\beta}}\frac{\left(V_{wind}^{19.5\mathrm{m}}\right)^2}{g} \tag{6}$$

where H_S comes from the area under the $S_{PM}(f)$ spectral function. The f_S and H_S values in (6) define a simplified mono-harmonic sea state, and in turn the hydrodynamic thrust F_{wave} via the well-known Morison equation (Morison et al., 1950; Vugts et al., 2001). This latter relates the drag and inertial components of the wave thrust, F_{wave}^D and F_{wave}^I, to the tower diameter D, the water depth d, the wave height H_S and the peak frequency f_S:

$$F_{wave}^D = \rho_w g \frac{C_d D}{8} H_S^2 \left(\frac{1}{2} + \frac{kd}{\sinh 2kd}\right) \qquad F_{wave}^I = \rho_w g \frac{C_m \pi D^2}{8} H_S \tanh kd \tag{7}$$

Similarly, the overturning drag and inertial moments with respect to the mudline read as:

$$\begin{aligned} M_{wave}^D &= \rho_w g \frac{C_d D}{8} H_S^2 \left[\frac{d}{2} + \frac{2(kd)^2 + 1 - \cosh 2kd}{4k \sinh 2kd}\right] \\ M_{wave}^I &= \rho_w g \frac{C_m \pi D^2}{8} H_S d \left[\tanh kd + \frac{1}{kd}\left(\frac{1}{\cosh kd - 1}\right)\right] \end{aligned} \tag{8}$$

In Equations (7)–(8), ρ_w denotes the water density and k the wave number related to f_S, whereas $C_d = 0.65$ and $C_m = 1.6$ are the drag and inertia coefficients suggested by the American Petroleum Institute (Journée and Massie, 2000). Since the drag and the inertial components of the wave force/moment are out of phase, the amplitudes of the force/moment resultants, F_{wave} and M_{wave}, are estimated via simplified SRSS averaging (Square Root of the Sum of the Squares). Finally, hydrodynamic loading can be globally represented as the following point load:

$$F_{wave}(t) = F_{wave} \sin(2\pi f_S t) = \sqrt{\left(F_{wave}^D\right)^2 + \left(F_{wave}^I\right)^2} \sin(2\pi f_S t) \tag{9}$$

applied at an elevation above the mudline equal to M_{wave}/F_{wave}.

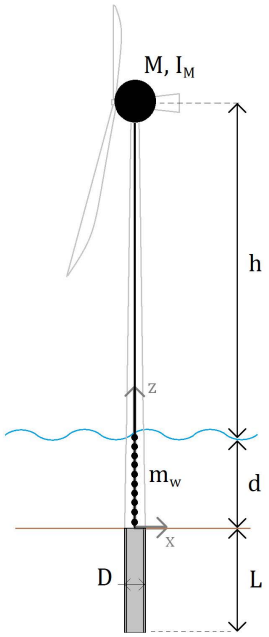

Figure 1: The reference 5 MW OWT (Jonkman et al., 2009)

3 Model set-up and performance

3.1 Structural model

All FE results relate to the same 5 MW OWT, defined according to Jonkman et al. (2009) and henceforth taken as a reference (Figure 1). The dynamic analysis of the OWT-monopile steel structure requires the setting of (Table 1):

- the diameter D, the length L and the wall thickness t of the tubular monopile ($L/D = 4$ and $t/D = 0.01$ are considered here);
- the OWT elevation h above the sea level and the water depth d;
- the mass density ρ_s of steel and its elastic properties (Young's modulus E_s and Poisson's ratio ν_s);
- the cross–sectional properties of the OWT tower modelled as a Timoshenko beam (see Section 2.2), i.e. the section area A_{sec} and the moment of inertia I_{sec} with respect to the horizontal y axis. Constant A_{sec} and I_{sec} are assumed along the OWT tower;
- the inertial properties of the hub-nacelle assembly, including the total (lumped) mass M and the rotational inertia I_M associated with the nacelle mass imbalances in the xz plane;
- the sea water mass participating in the OWT vibration. Following Newman (1977), this effect is incorporated by introducing an added water mass equal to:

$$m_w = 2\rho_w \frac{\pi D^2}{4} d \tag{10}$$

and evenly distributed along the underwater beam nodes of the OWT (Figure 1).

[3] $V_{wind}^{19.5\text{m}}$ can obtained from the anemometric value V_{wind} by assuming for the wind speed a power law (or more complicated) distribution along the elevation (Panofsky and Dutton, 1984; Hsu et al., 1994).

Table 1: Geometrical and mechanical properties of the OWT–monopile structure

h [m]	d [m]	L [m]	D [m]	t [cm]	ρ_s [ton/m^3]	E_s [GPa]	ν_s [-]	A_{sec} [m^2]	I_{sec} [m^4]	M [ton]	I_M [ton·m^2]	m_w [ton]
90	20	20	5	5	7.85	200	0.3	0.7776	2.3818	350	2600	785

Table 2: HM soil parameters (Yang and Elgamal, 2008)

Parameter	Unit	Value
reference shear modulus G_r	[kPa]	1×10^5
reference bulk modulus K_r	[kPa]	1.7×10^5
reference effective confinement p'_r	[kPa]	100
pressure dependence coefficient n	[–]	0.5
friction angle ϕ'	[deg]	35.5
shear strain γ_{max} at peak strength	[–]	0.085
phase transformation angle ϕ_{PT}	[deg]	31
contraction parameter c_1	[–]	0.125
contraction parameter c_2	[–]	0.5
contraction parameter c_3	[–]	1
dilation parameter d_1	[–]	0.25
dilation parameter d_2	[–]	3.9
dilation parameter d_3	[–]	5.7
liquefaction strain parameter p'_y	[–]	1.95
liquefaction strain parameter $\gamma_{s_{max}}$	[–]	0
saturated mass density ρ	[ton/m^3]	1.8
Darcy permeability k	[m/s]	5×10^{-4}

3.2 Soil parameters

The reference 5 MW OWT is assumed to interact with a homogeneous sand deposit. In order to generate a realistic soil response, the UCSD08 soil parameters have been calibrated against real laboratory test results, concerning a siliceous medium dense sand (relative density $D_R \approx 60\%$) from an offshore site in Myanmar (courtesy of D'Appolonia S.p.A.). The experimental tests were performed on sand specimens sampled at 20 m depth below the mudline, then subjected to anisotropic consolidation and triaxial shearing. Figure 2 displays the comparison between experimental results and UCSD08 simulations for monotonic[4] (Figure 2a-b-c) and cyclic[5] undrained triaxial tests in terms of (i) effective stress path, (ii) stress–strain response and (iii) pore pressure evolution.

The UCSD08 parameters identified as suggested by Yang et al. (2003) are listed in Table 2. The UCSD08 model can quite accurately reproduce the experimental test results, although the overpredicted accumulation of cyclic axial strain (*ratcheting*) should also be noticed (Figure 2e). The latter is a genuine, poorly documented outcome of many existing cyclic models under non-symmetric load cycles (di Prisco and Mortara, 2013; Corti et al., 2016).

Soil–monopile interface The discontinuity in hydro-mechnical properties at the soil-monopile interface is handled according to the approach by Griffiths (1985), i.e. by inserting a thin layer of solid (ssp) elements to model the physical transition from steel to soil. The interface layer is as

[4] the initial vertical (σ'_{v0}) and radial (σ'_{h0}) effective stresses equal 187 and 90 kPa, respectively, then axial loading is applied with a displacement rate equal to 0.02 mm/min.

[5] a ±140 kPa cyclic variation in vertical (total) stress is applied at 0.25 Hz starting from $\sigma'_{v0} = 155$ kPa and $\sigma'_{h0} = 60$ kPa.

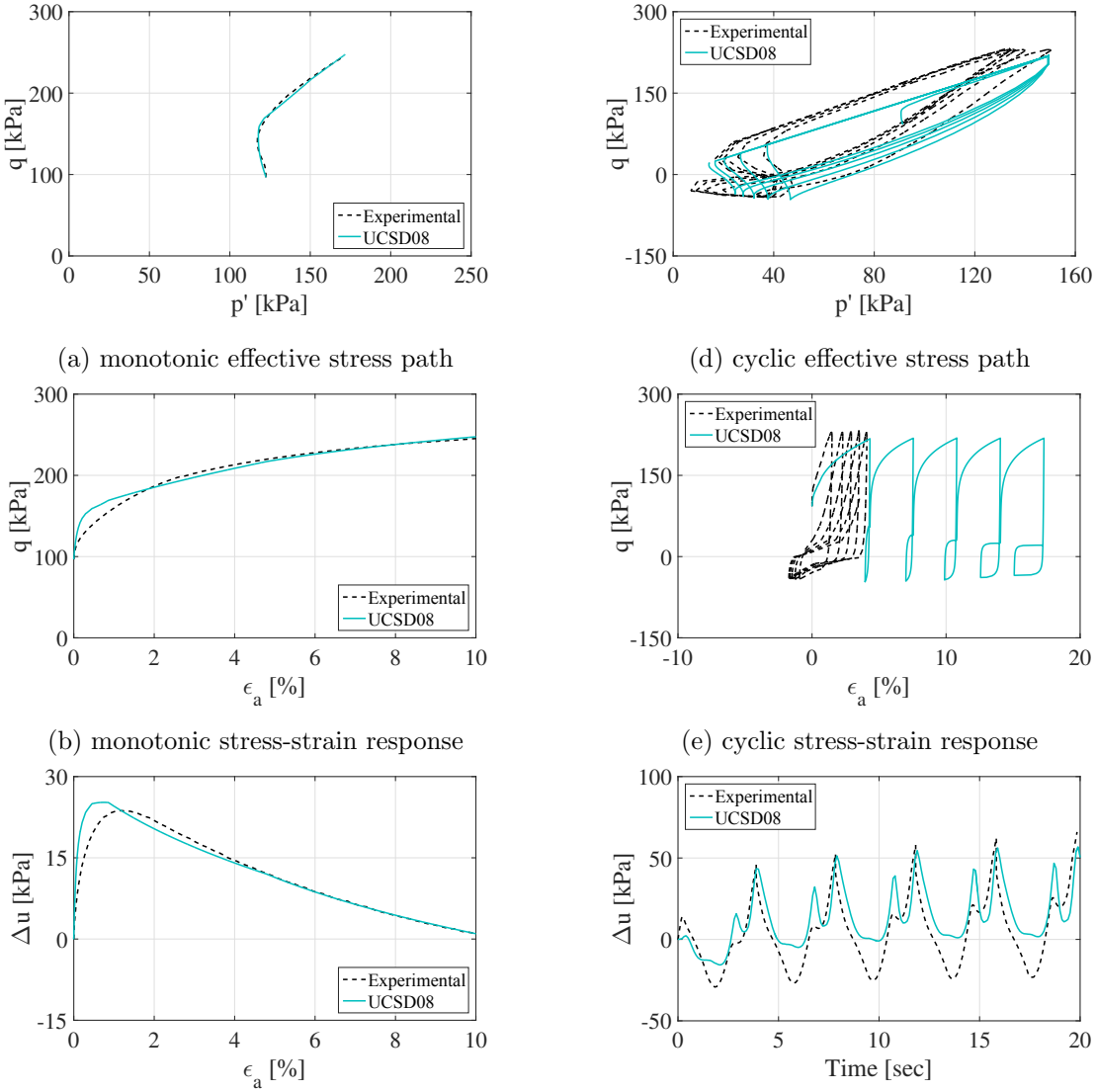

(a) monotonic effective stress path

(d) cyclic effective stress path

(b) monotonic stress-strain response

(e) cyclic stress-strain response

(c) monotonic pore pressure build-up

(f) cyclic pore pressure build-up

Figure 2: Monotonic and cyclic triaxial response of medium dense sand specimens: comparison between experimental data (courtesy of D'Appolonia S.p.A) and UCSD08 simulations

thick as 4% of the monopile diameter and is assumed to behave as a UCSD08 saturated material. Specifically, the frictional angles mobilised at phase transformation and shear failure, ϕ_{PT} and ϕ', are set to 2/3 of the values in Table 2 to create a more deformable interface material.

3.3 Size and space discretization of the FE model

Appropriate size and space discretization for the soil FE domain around the monopile have been selected based on the preliminary tests documented in Appendix A. Figure 3 illustrates the final soil domain discretised with approximately 6000 ssp bricks. Since only one lateral loading direction is considered (along the x axis in Figure 3), geometrical and loading symmetries are exploited to reduce the high computational costs for 3D FE computations. The halved FE model features $Z/L = 1.5$, $W/L = 1.75$ and $W/D = 7$, with Z, W, L, D defined as in Figure 3.

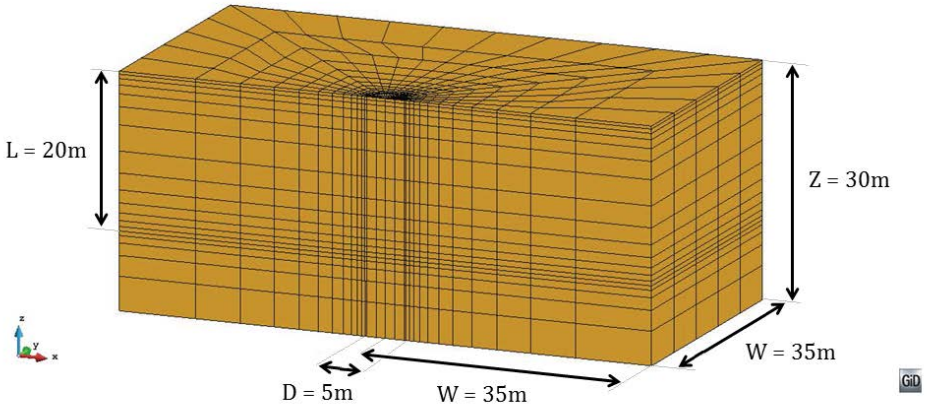

Figure 3: Soil domain and ssp FE discretisation

3.4 Loading stages and boundary conditions

All the numerical simulations are performed according to the following loading stages.

Soil gravity loading At the very beginning, the FE model only includes soil elements (no structural members), initially at rest and unloaded. Then, the self-weight of the soil-water mixture is applied in increments to generate initial stress and pore pressure distributions. As for mechanical boundary conditions, the displacement components normal to the bottom and the lateral surfaces of the soil box in Figure 3 are prevented, while the top surface is free. The same soil box is hydraulically impermeable along all its boundaries but at the top surface, where excess pore pressures are prevented.

OWT installation The simulation of monopile installation procedures is not a goal of this work, where the traditional "wished-in-place" approach is conversely followed. The monopile-OWT structure is introduced into the FE model by removing two-phase soil elements in the pile zone and replacing them with mono-phase elements. In order to accommodate this replacement, the nodes at two-phase–mono-phase contact are duplicated and connected only through displacement components in a so-called "master-slave" fashion, automatically making the monopile surface impermeable to water flow. After the monopile is created, the above-mentioned rigid links between the pile head and the lower OWT nodes are introduced.

Transient analysis The dynamic response of the soil-monopile-OWT system is finally simulated by modifying the above boundary conditions as follows:

1. the nodal fixities at the lateral/bottom surfaces of the soil domain are replaced by viscous dashpots[6] to damp out outgoing waves (Lysmer and Kuhlemeyer, 1969);

2. point forces at preselected nodes of the OWT beam are applied to model wind/wave loading.

As discussed in Appendix A, dynamic simulations are performed by setting the values $\Delta t = 0.004\,\mathrm{s}$ and $\alpha = 6 \times 10^{-6}$ for the time step-size and the ssp stabilisation parameter in Equation (3), respectively.

[6]The viscous parameters of the boundary dashpots are set by accounting for the effect of water saturation on the propagation velocity of compressional P waves (Foti et al., 2002).

3.5 Features of soil-monopile-OWT dynamics

This section illustrates the predictive potential of the soil-monopile-OWT FE model. For this purpose, a point load is applied to the OWT hub (Figure 4a) and the resulting transient response numerically simulated. The following loading time history is considered (Figure 4b):

$$H(t) = \begin{cases} 0 \le t \le T_0: & H^{max} \sin(2\pi f t) \\ T_0 < t \le T_f: & 0 \end{cases} \tag{11}$$

with $H^{max} = 1\,\text{MN}$, $f = 0.5\,\text{Hz}$, $T_0 = 8\,\text{s}$ and $T_f = 30\,\text{s}$. All soil parameters are listed in Table 2.

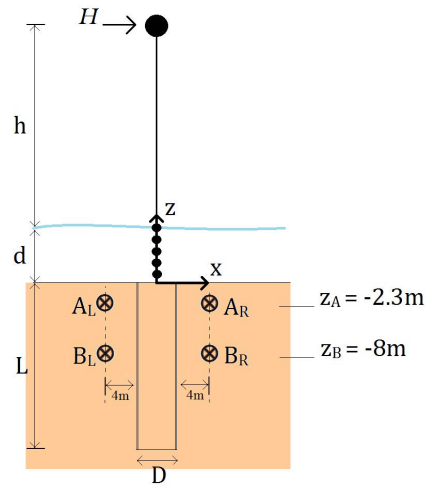

(a) vertical section $(x, y = 0, z)$

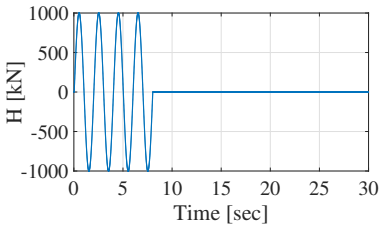

(b) load time history

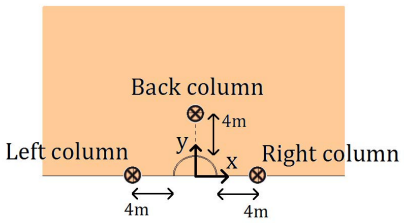

(c) horizontal section $(x, y, z = 0)$

Figure 4: Point-loaded OWT and control locations defined for plotting purposes

HM soil response around the monopile Variations in stresses, strains and pore water pressure are recorded in the FE soil domain while the OWT vibrates. The predicted excess pore pressure Δu is plotted against time in Figures 5a-5b for the four control points $A_{L,R}$ and $B_{L,R}$ (Figure 4a); Figures 5c-5d illustrate normalised pore pressure isochrones for the three nodal columns in Figure 4c at times $t = 5$, 10 s.

At the considered locations, Δu evolves in time depending on (i) variations in total mean stress p, (ii) water drainage (drained, partially drained or undrained response) and (iii) soil volume changes under shear loading. In particular, the results in Figure 5 suggest that:

- the sign of the excess pore pressure is mostly governed by the current position of the vibrating monopile. Under "passive-like" conditions (the pile is intruding into the soil), the total mean confinement tends to increase and positive Δu arises. At the same time, negative Δu is recorded on the opposite side of the monopile ("active-like" conditions);
- the portion of Δu induced by volumetric-deviatoric coupling is typically negative in medium dense sands (Section 3.2). Therefore, the two interplaying pressure generation mechanisms give rise to Δu oscillations with more pronounced negative peaks.
- pressure isochrone patterns evolve as the OWT transits from forced ($t \le T_0$) to free/damped ($t > T_0$) vibration. The smooth pressure isochrones testify the effectiveness of the ssp stabilisation (McGann et al., 2015).

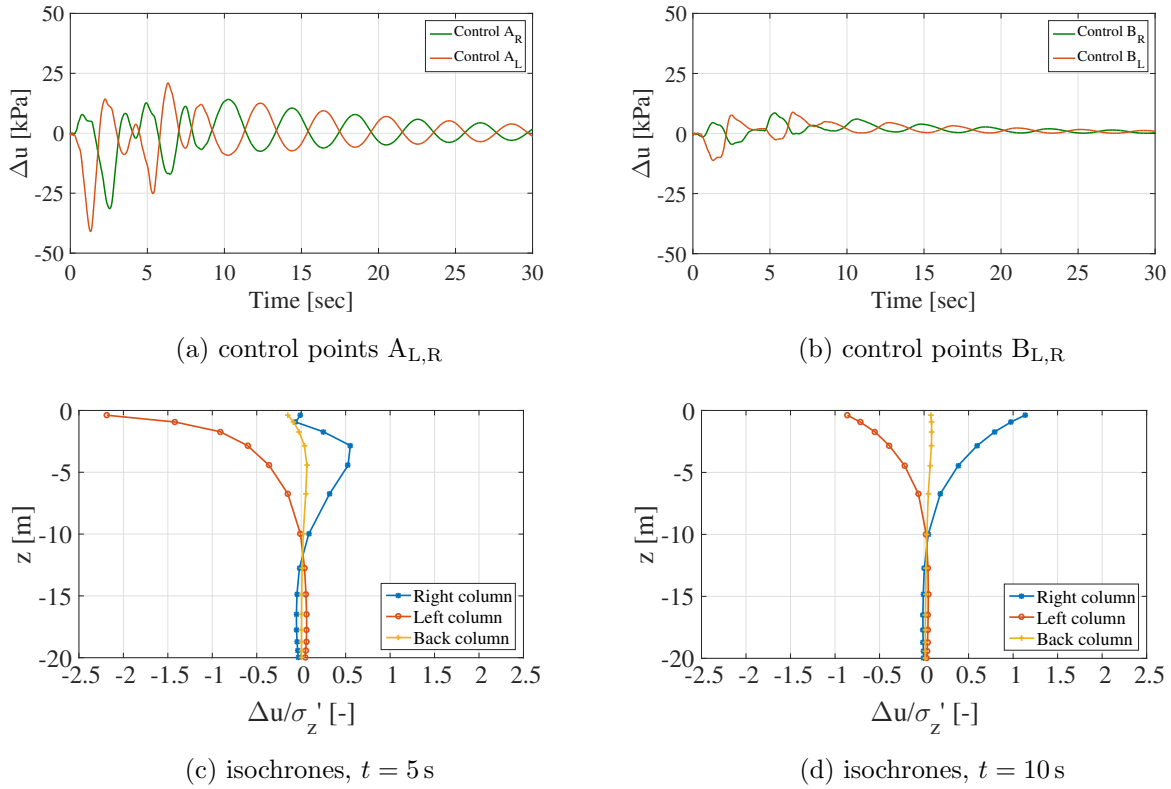

(a) control points $A_{L,R}$

(b) control points $B_{L,R}$

(c) isochrones, $t = 5\,\mathrm{s}$

(d) isochrones, $t = 10\,\mathrm{s}$

Figure 5: Time evolution and isochrones of excess pore pressure at the locations in Figure 4

The pore pressure evolution is obviously linked to the mechanical response of the soil, here represented in terms of shear stress-strain curves (Figure 6) and effective stress paths (Figure 7) at points $A_{L,R}$ and $B_{L,R}$. If the $\tau_{xz} - p'$ stress paths cross the phase transformation line during shear loading, then the effective mean pressure p' increases due to negative excess pore pressure and, as a consequence, higher shear stresses can be borne by the soil. This contradicts a common misconception: soil non-linearity does not always imply softer response and lower strength, but the opposite may be true in presence of dilative granular materials.

Vibrational response of the monopile-OWT structure The dynamic response of the monopile-OWT structure is visualised in Figure 8 in both time and frequency domains. The displacement time histories simulated at the OWT hub and monopile head are plotted in Figure 8a-8b. While the monopile head displaces much less than the hub, the comparison to the hub response predicted by a simpler clamped OWT model (grey line) points out the quantitative significance of the foundational compliance.

The frequency domain performance is shown in Figure 8c in terms of numerical frequency response function (FRF) at the OWT hub mass (Fourier amplitude ratio between the inertia force – mass times acceleration – and the input load). The numerical FRF (blue solid line) is also interpolated with the analytical FRF of a visco-elastic single-degree-of-freedom (1DOF) oscillator (grey dashed line):

$$FRF = \frac{1}{\sqrt{(1 - f/f_0)^2 + (2\xi f/f_0)^2}} \tag{12}$$

where f_0 denotes the natural frequency and ξ the damping ratio (Chopra, 1995). Although the analytical-numerical comparison is only reliable around f_0[7], realistic natural frequency and

[7]Numerical spectral ratios are meaningless at frequencies associated with negligible input spectral amplitudes –

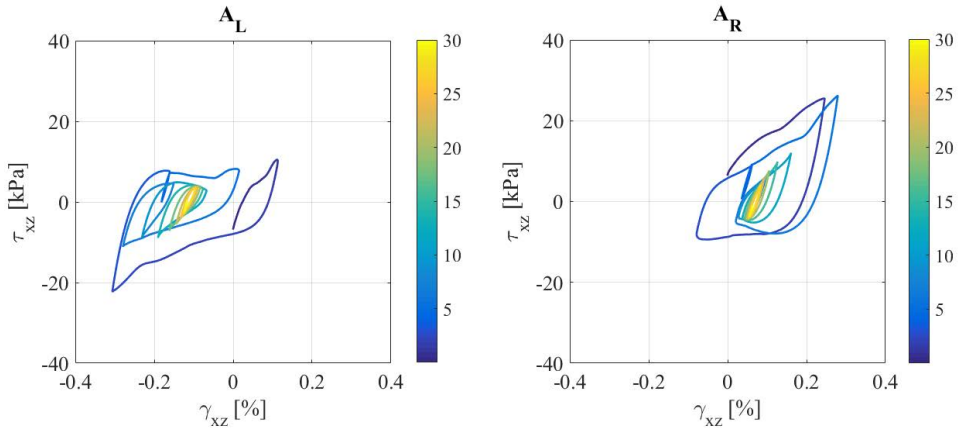

(a) control points $A_{L,R}$

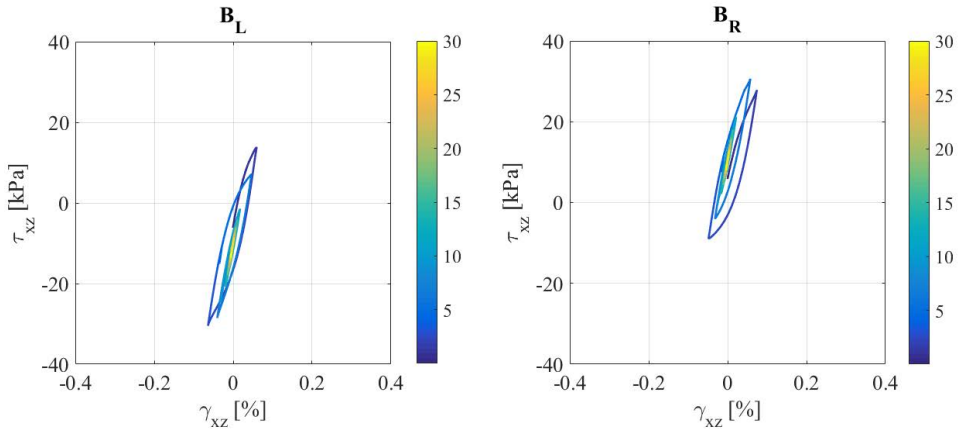

(b) control points $B_{L,R}$

Figure 6: Shear stress-strain response at the control points defined in Figure 4. The colorbars indicate the time elapsing from 0 to 30 s.

damping ratio are estimated – 0.243 Hz and 6.5%, respectively. ξ is correctly larger than the 5% value set for the OWT beam (Section 2.2), as it also includes the energy dissipation due to soil plasticity and wave radiation.

3.6 Role of the soil volumetric behaviour

The results of a purely numerical experiment are reported to stress the structural implications of the soil volumetric behaviour. For this purpose, the UCSD08 model is first recalibrated by keeping the parameters in Table 2 and resetting $\phi_{PT} = \phi'$. Figure 9a displays the effect of this recalibration in terms of undrained soil response to symmetric triaxial loading: while the previous parameter calibration gave rise to the typical behaviour of dilative sands (blue line), the new calibration results in a liquefying response (green line).

Figure 9b illustrates the FRFs obtained for two identical OWTs, one funded in the dilative sand and the other in its "virtual" compactive counterpart. The transition from dilative to compactive sand behaviour is itself responsible for a 2% reduction in f_0 (from 0.243 Hz to 0.239 Hz), not negligible in the context of offshore wind applications. As discussed in different research contexts

in Figure 8c, at frequencies out of the 0.2–0.3 Hz range.

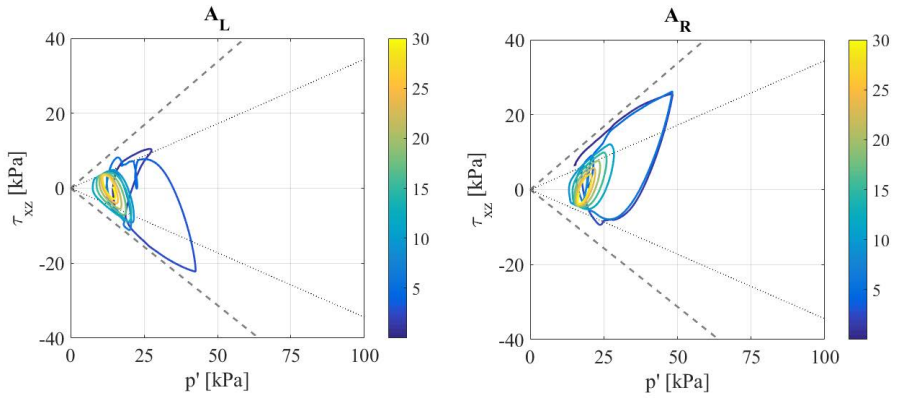

(a) control points $A_{L,R}$

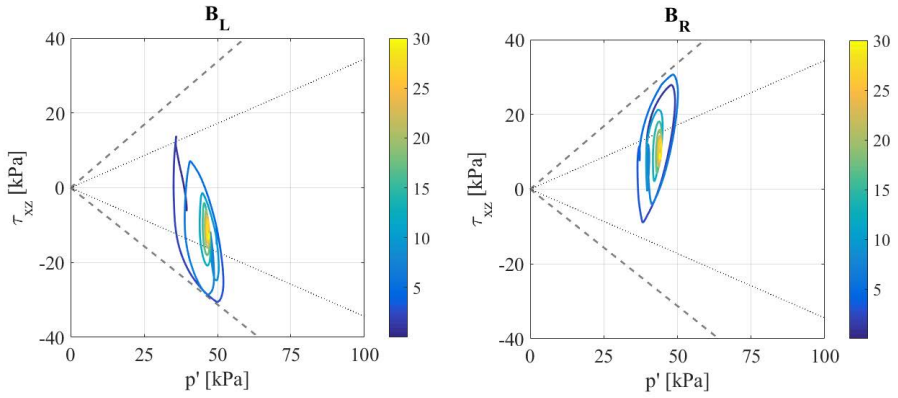

(b) control points $B_{L,R}$

Figure 7: Effective stress paths at the control points defined in Figure 4. Failure (dashed lines) and phase transformation (dotted lines) loci are also plotted. The colorbars indicate the time elapsing from 0 to 30 s.

(Iai et al., 1995; Elgamal et al., 2005; Bonilla et al., 2005; Roten et al., 2013), soil dilation can give rise to stiffer soil responses under both undrained and drained conditions: in the former case, the development of negative excess pore pressure enhances the effective confinement around the monopile; in the latter, higher confining stresses result from prevented volume expansion.

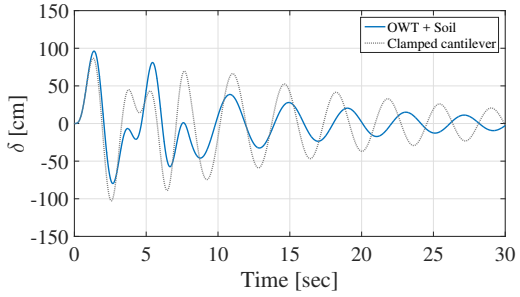

(a) hub

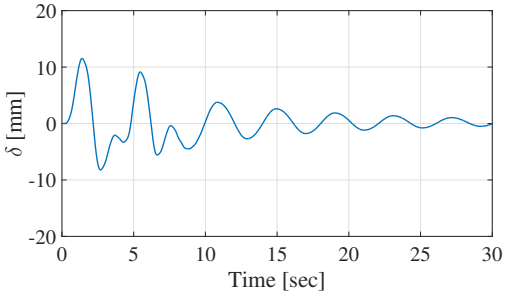

(b) monopile head (mudline)

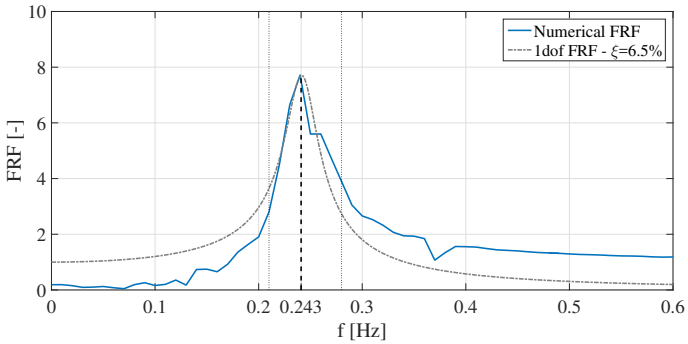

(c) FRF at the OWT hub and 1DOF analytical interpolation

Figure 8: Dynamic response of the monopile-OWT structure

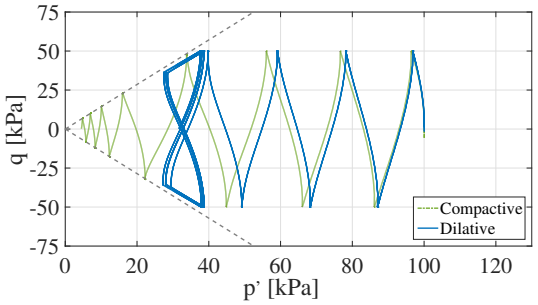

(a) dilative and compactive calibrations of the UCSD08 flow rule

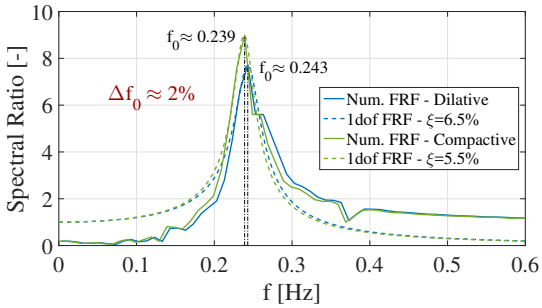

(b) numerical FRFs and 1DOF interpolations

Figure 9: Relation between soil volume changes and OWT dynamics: dilative vs compactive plastic flow rules

4 OWT response to environmental loading

The OWT response to more realistic environmental loading is discussed in the following. Structural specifications, soil properties and analysis parameters are as in the previous sections.

4.1 Loading scenarios

The wind/wave thrust forces depicted in Figure 10 are determined as described in Section 2.3. For this purpose, four different anemometric records are considered to represent typical wind conditions in the Irish Sea (courtesy of Siemens Wind Power). Four realistic loading scenarios – corresponding to average wind speeds V_{wind}^{avg} of approximately 5, 10, 15, 20 m/s (cases A, B, C,

D) – are generated as follows:

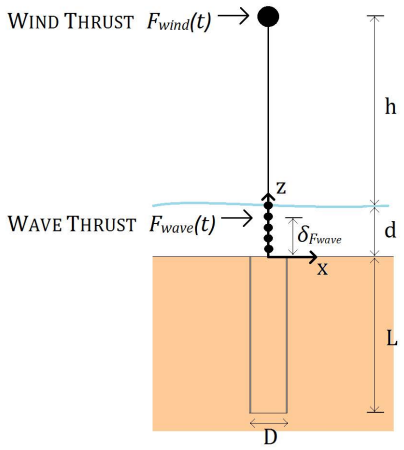

Figure 10: OWT subjected to wind/wave point loads

1. wind velocity records (total duration: 600 s) are first reduced to 30 s time histories for computational convenience. Then, wind velocities are directly converted into wind thrust forces via the BEM Equation (4);

2. the PM wave spectrum is computed for the considered OWT structure and water depth (Figure 10), then the main wave frequency f_S and the corresponding wave height H_S are obtained. For given f_S, H_S and structural specifications, the wave thrust forces and their application points $\delta_{F_{wave}}$ (elevation with respect to the mudline) are determined through Equations (7)-(8).

The resulting wind/wave load histories are plotted in Figure 11, while the corresponding load parameters are listed in Table 3. As can be noted, wind and wave forces are gradually applied through a 5 s ramp to avoid failure of FE simulations due to sudden load application.

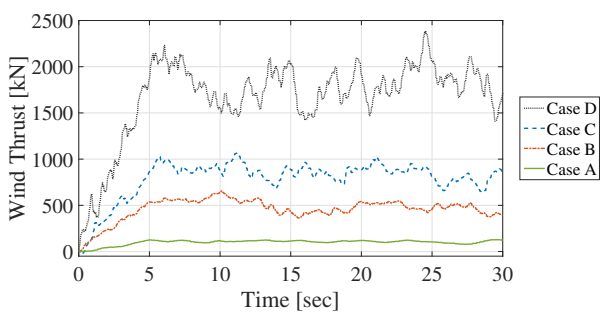

(a) wind

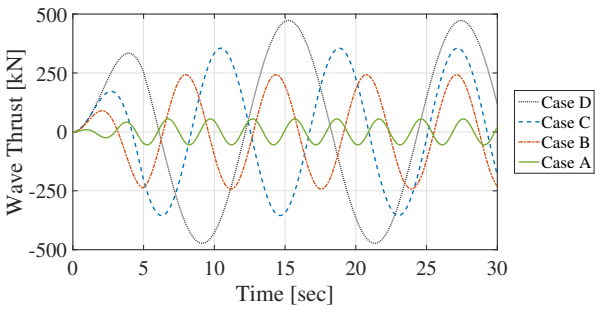

(b) waves

Figure 11: Wind/wave thrust time histories

4.2 Numerical results

The main numerical outcomes are illustrated for the above loading cases in terms of soil–monopile interaction (Section 4.2.1) and OWT dynamics (Section 4.2.2). For all V_{wind}^{avg} scenarios, the soil

Table 3: Wind/wave load specifications for the four wind speed scenarios

	V_{wind}^{avg} [m/s]	F_{wind}^{avg} [kN]	f_S [Hz]	H_S [m]	F_{wave}^{max} [kN]	$\delta_{F_{wave}}$ [m]
Case A	4.83	109	0.336	0.36	±55	17.8
Case B	10.34	500	0.157	1.64	±243	12.3
Case C	13.56	860	0.120	2.81	±355	11.0
Case D	19.76	1820	0.082	5.97	±473	10.3

permeability is gradually varied in order of magnitude within the $10^{-2} - 10^{-7}$ m/s range (k values are thus regularly spaced on a logarithmic scale).

4.2.1 Soil–monopile interaction

Figure 12 shows the simulated displacement response of the monopile head at varying soil permeability. The maximum displacement – and its unrecoverable component – increases substantially at larger V_{wind}^{avg}, with higher pile deflections predicted as the drained limit is approached ($k \to 10^{-2}$ m/s). While the prevention of soil volume changes is expected to affect the monopile displacements, soil permeability does not seem to influence the oscillation frequency at the monopile head. It should be also noted that the transition from the undrained to the drained limit is affected by V_{wind}^{avg}: as more soil non-linearity is mobilised at increasing V_{wind}^{avg}, higher permeabilities are needed for a fully drained response.

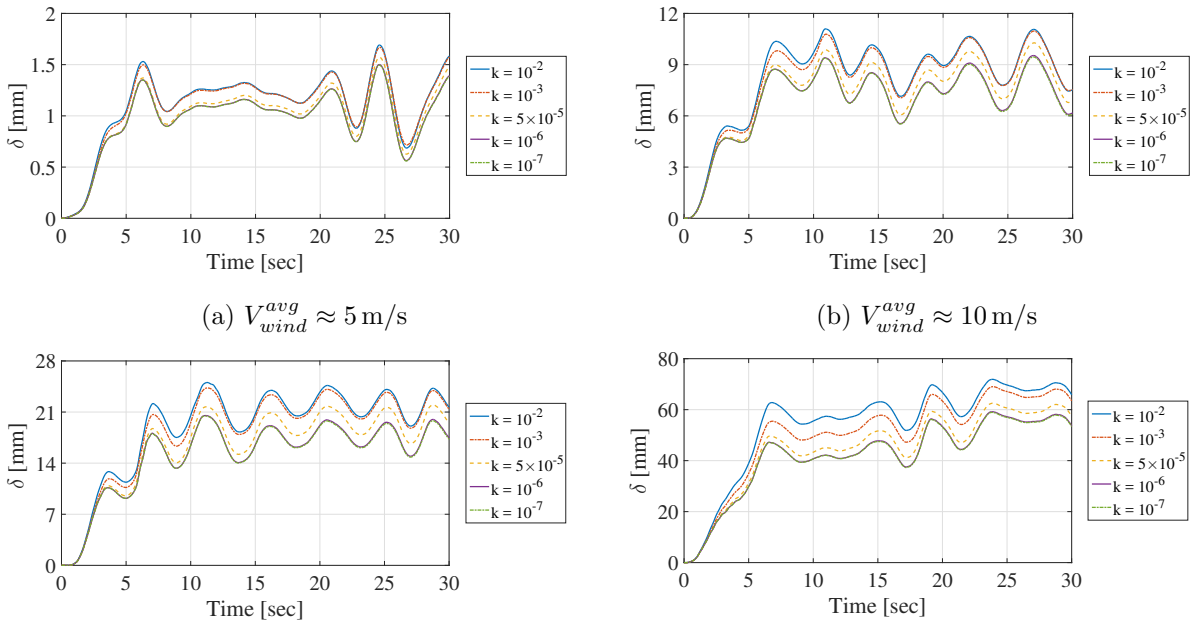

(a) $V_{wind}^{avg} \approx 5\,\text{m/s}$ (b) $V_{wind}^{avg} \approx 10\,\text{m/s}$

(c) $V_{wind}^{avg} \approx 15\,\text{m/s}$ (d) $V_{wind}^{avg} \approx 20\,\text{m/s}$

Figure 12: Displacement response of the monopile head (mudline) at varying soil permeability k [m/s]

Figure 13 highlights the relationship between soil strains and V_{wind}^{avg}. The deviatoric strain patterns around the monopile suggest that severe soil strains (larger than 0.1%) may not arise when $V_{wind}^{avg} < 10$ m/s. Further, although significant plastic straining occurs at the largest load amplitude ($V_{wind}^{avg} \approx 20\,\text{m/s}$), only a small amount of the total lateral capacity is mobilised. This is clearly illustrated in Figure 14, where the shear force time history at the monopile head (Figure

14a) is compared to the lateral load-displacement curve obtained through static pushover (solid line in Figure 14b). For verification purposes, the simulated lateral response is plotted along with the stiffer curve obtained by Abdel-Rahman and Achmus (2005) for a larger monopile ($D = 7.5\,\mathrm{m}$ and same length $L = 20\,\mathrm{m}$).

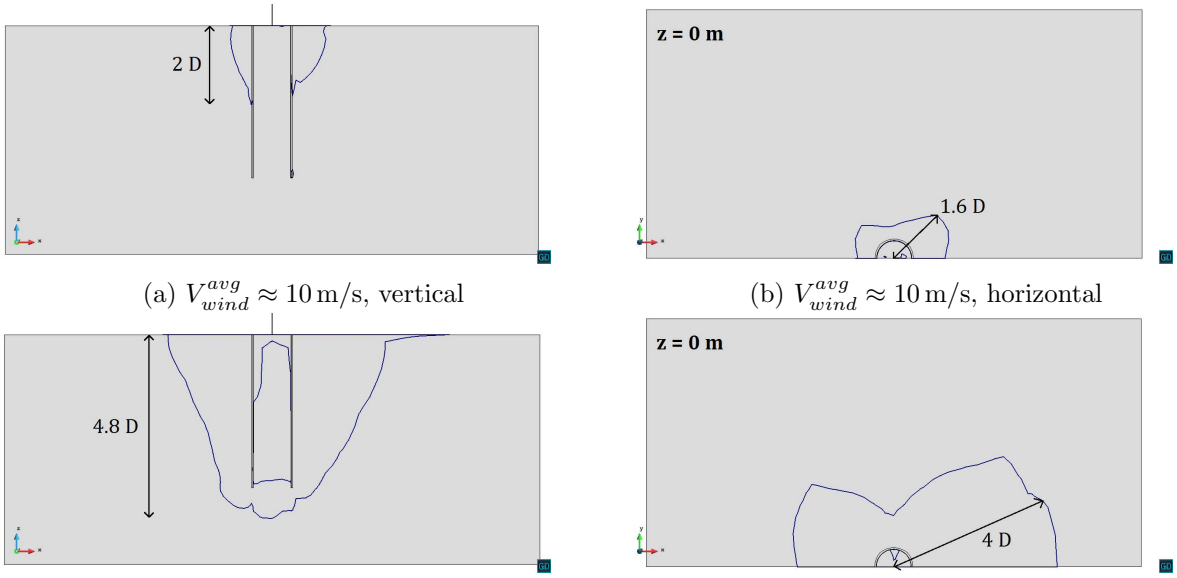

(a) $V_{wind}^{avg} \approx 10\,\mathrm{m/s}$, vertical

(b) $V_{wind}^{avg} \approx 10\,\mathrm{m/s}$, horizontal

(c) $V_{wind}^{avg} \approx 20\,\mathrm{m/s}$, vertical

(d) $V_{wind}^{avg} \approx 20\,\mathrm{m/s}$, horizontal

Figure 13: 0.1% deviatoric strain contour lines – vertical $(x, y = 0, z)$ and horizontal $(x, y, z = 0 -$ mudline) sections (soil permeability: $k = 10^{-6}\,\mathrm{m/s}$)

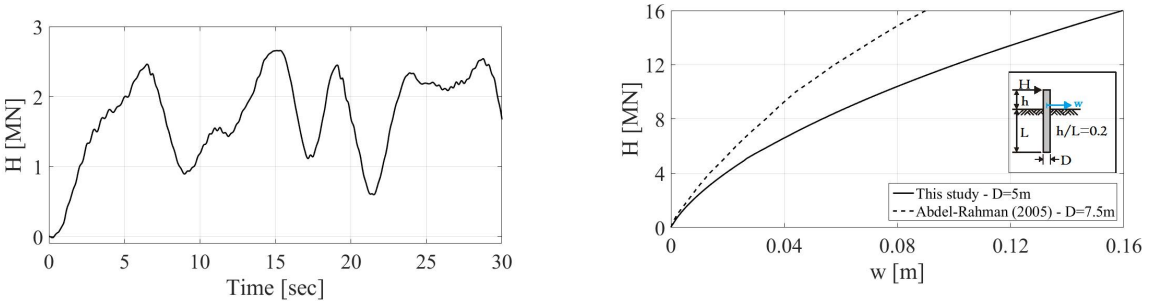

(a) shear force time history

(b) lateral load-displacement curve (comparison with Abdel-Rahman and Achmus (2005))

Figure 14: Lateral response of the monopile head at $V_{wind}^{avg} \approx 20\,\mathrm{m/s}$

4.2.2 OWT natural frequency

Figure 15 shows the displacement response of the OWT hub to the load scenarios A, B, C and D at varying permeability; the results are also compared to the predictions for an OWT clamped at the mudline (grey lines). As observed in Figure 8a, the presence of a compliant foundation affects significantly the global response and the natural frequency. On the other hand, soil permeability seems to negligibly impact the hub displacement (in the order of tens of centimeters), even though its influence has been clearly observed at the monopile head for medium-large wind speeds (Figure 12). These two observations are not in contradiction after considering the 100 m distance between the mudline and the OWT hub: the magnitude of the OWT displacement is dominated by the

structural flexibility, so that relatively slight variations in monopile deflection do not produce severe effects at the top of the wind tower.

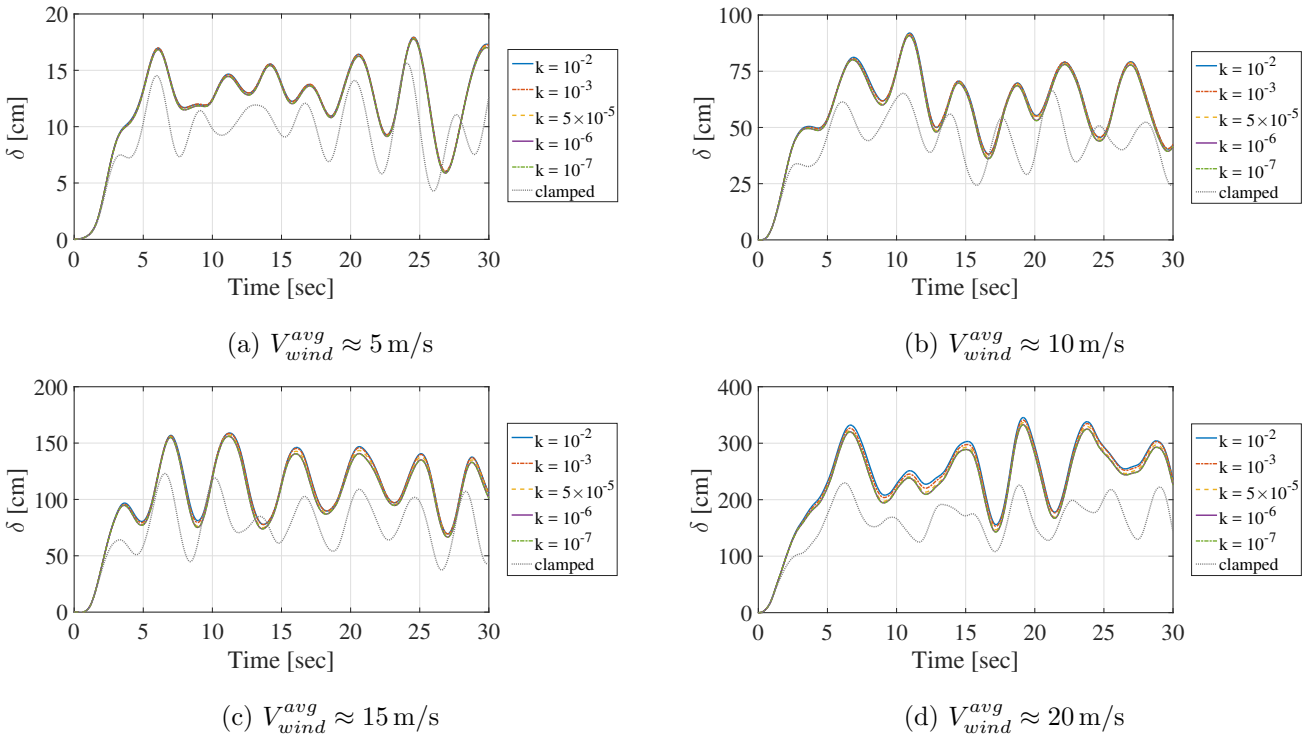

(a) $V_{wind}^{avg} \approx 5\,\mathrm{m/s}$ (b) $V_{wind}^{avg} \approx 10\,\mathrm{m/s}$

(c) $V_{wind}^{avg} \approx 15\,\mathrm{m/s}$ (d) $V_{wind}^{avg} \approx 20\,\mathrm{m/s}$

Figure 15: Displacement response of the OWT hub at varying soil permeability k [m/s]

The same inference is supported by Figure 16, where the power spectral density (PSD) of the hub displacement is plotted after normalisation by the maximum value ($0 \leq PSD \leq 1$) – the spectral peaks ($PSD = 1$) identify the OWT natural frequency f_0. f_0 is compared in Figure 16 to the natural frequencies computed for (i) clamped OWT (circular marker) and (ii) OWT in linear elastic soil[8] (square marker). Unlike the clamped and the linear elastic f_0 values, the "non-linear" natural frequency varies in relation to the load amplitude (V_{win}^{avg}) and the following features of sand behaviour: (i) sand stiffness increases at larger effective confinement p'; (ii) sand stiffness decreases under shear straining; (iii) volume HM effects in dilative sands result in higher shear stiffness. In light of these observations, it is possible to explain the observed variations in f_0:

(a) $V_{wind}^{avg} \approx 5$ m/s – low soil plasticity is mobilised, so that the global response is mostly non-linear elastic. The local variations in effective confinement make the sand stiffer than it is immediately after gravity loading (Section 3.4), and f_0 gets closer to the clamped value;

(b) $V_{wind}^{avg} \approx 10$ m/s – as the load amplitude increases, deviatoric straining implies lower sand stiffness and f_0;

(c) $V_{wind}^{avg} \approx 15$ m/s – the soil shear stiffness and f_0 keep decreasing;

(d) $V_{wind}^{avg} \approx 20$ m/s – substantial soil plasticity and HM volume effects are triggered. In dilative sands, these are expected to stiffen the soil, and indeed a slight increase in f_0 is noted. This finding confirms what inferred from Figure 9.

[8]The linear elastic f_0 has been determined by inhibiting soil plastic strains and recording the OWT free vibrations induced by a very small initial load (10 kN, not inducing substantial variations in the soil elastic moduli).

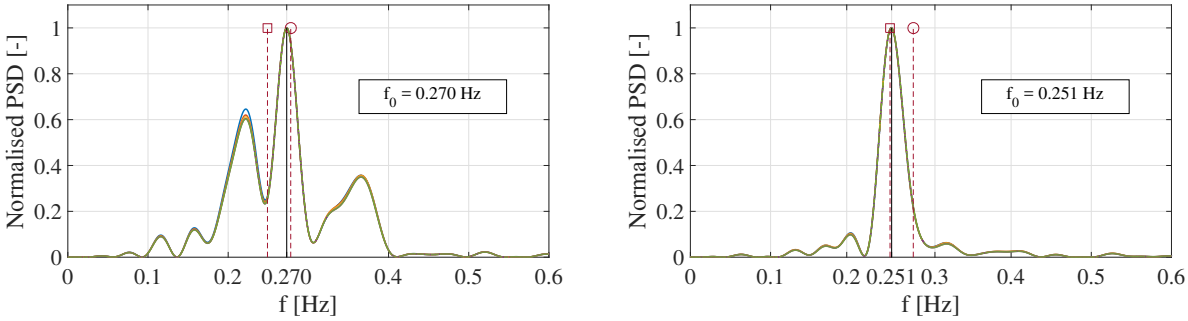

(a) $V_{wind}^{avg} \approx 5\,\mathrm{m/s}$ (b) $V_{wind}^{avg} \approx 10\,\mathrm{m/s}$

(c) $V_{wind}^{avg} \approx 15\,\mathrm{m/s}$ (d) $V_{wind}^{avg} \approx 20\,\mathrm{m/s}$

Figure 16: Normalised displacement power spectra for the OWT hub at varying soil permeability. The circular and the square markers denote the f_0 associated with a clamped OWT and an OWT in a linear elastic sand, respectively.

5 Concluding remarks

A 3D HM FE model was developed for the time-domain analysis of environmentally loaded OWTs, accounting for (i) slow soil dynamics, (ii) pore pressure effects and (iii) non-linear cyclic soil behaviour. Specifically, the well-known u-p formulation was adopted in combination with the UCSD08 soil model, while the computational efficiency was globally enhanced by exploiting the very recent equal-order H1-P1ssp element formulation.

A standard 5 MW OWT was analysed under four wind speed scenarios ($V_{wind}^{avg} \approx 5, 10, 15, 20$ m/s) and with soil permeability varying from 10^{-2} m/s to 10^{-7} m/s. Although real site conditions (e.g. in the North Sea) would include stratigraphic inhomogeneity, a typical 5 MW OWT in a homogeneous medium dense sand layer was considered. The numerical results allowed to gain insight into some relevant geotechnical aspects:

- soil non-linearities may become particularly influential at wind speeds larger than 10 m/s;
- at medium-large loading levels, the pore pressure regime has clear influence on monopile displacements, but negligibly affects the OWT response at the hub (and therefore the natural frequency);
- the OWT natural frequency results from the complex interplay of loading amplitude and non-linear/dilatancy effects in the soil. More soil non-linearity does not necessarily imply a monotonic decrease of the natural frequency.

Future developments along this research line will aim to improve model reliability in terms of (i) cyclic soil modelling (void ratios effects and ratcheting), (ii) site inhomogeneity (layering) and

(iii) environmental loading (longer time histories and more complex loading combinations). The goal is to keep providing more solid ground for reviewing current design methods on the basis of integrated FE modelling.

Acknowledgements

D'Appolonia S.p.A (San Donato Milanese, Italy) and Siemens Wind Power (The Hague, The Netherlands) are gratefully acknowledged for providing real data from laboratory soil tests and anemometric measurements, respectively. Warm thanks also go to Pim Versteijlen (TU Delft/Siemens Wind Power) and Frank Renting (TU Delft) for their useful suggestions on the modelling of OWT structures and environmental loads.

References

Abdel-Rahman, K. and Achmus, M. (2005). Finite element modelling of horizontally loaded monopile foundations for Offshore Wind Energy Converters in Germany. In *Proceedings of the International Symposium on Frontiers in Offshore Geotechnics. Perth, WA, Australia*, pages 391–396.

Achmus, M., Kuo, Y.-S., and Abdel-Rahman, K. (2009). Behavior of monopile foundations under cyclic lateral load. *Computers and Geotechnics*, 36(5):725–735.

Arany, L., Bhattacharya, S., Macdonald, J. H. G., and Hogan, S. J. (2016). Closed form solution of eigenfrequency of monopile supported offshore wind turbines in deeper waters incorporating stiffness of substructure and SSI. *Computers and Geotechnics*, 83:18–32.

Arapogianni, A., Genachte, A.-B., et al. (2013). Deep water: the next step for offshore wind energy. Technical report, European Wind Energy Association. Brussels, Belgium.

Babuška, I. (1973). The finite element method with Lagrangian multipliers. *Numerische Mathematik*, 20(3):179–192.

Bhattacharya, S., Cox, J. A., Lombardi, D., and Wood, D. M. (2013). Dynamics of offshore wind turbines supported on two foundations. *Proceedings of the Institution of Civil Engineers: Geotechnical Engineering*, 166:159–169.

Bienen, B., Dührkop, J., Grabe, J., Randolph, M. F., and White, D. J. (2011). Response of piles with wings to monotonic and cyclic lateral loading in sand. *Journal of Geotechnical and Geoenvironmental Engineering*, 138(3):364–375.

Bonilla, L. F., Archuleta, R. J., and Lavallée, D. (2005). Hysteretic and dilatant behavior of cohesionless soils and their effects on nonlinear site response: Field data observations and modeling. *Bulletin of the Seismological Society of America*, 95(6):2373–2395.

Brezzi, F. (1974). On the existence, uniqueness and approximation of saddle-point problems arising from Lagrangian multipliers. *Revue française d'automatique, informatique, recherche opérationnelle. Analyse numérique*, 8(2):129–151.

Byrne, B. W., McAdam, R. A., Burd, H. J., Houlsby, G. T., Martin, C. M., Gavin, K., Doherty, P., Igoe, D., Zdravković, L., Taborda, D. M. G., et al. (2015a). Field testing of large diameter piles under lateral loading for offshore wind applications. In *Proceedings of the 16th European Conference on Soil Mechanics and Geotechnical Engineering. Edinburgh, UK*, pages 1255–1260.

Byrne, B. W., McAdam, R. A., Burd, H. J., Houlsby, G. T., Martin, C. M., Zdravković, L., Taborda, D. M. G., Potts, D. M., Jardine, R. J., Sideri, M., et al. (2015b). New design methods for large diameter piles under lateral loading for offshore wind applications. In *Proceedings of 3rd International Symposium on Frontiers in Offshore Geotechnics. Oslo, Norway*, pages 705–710.

Cheng, Z. and Jeremić, B. (2009). Numerical modeling and simulations of piles in liquefiable soil. *Soil Dynamics and Earthquake Engineering*, 29(11-12):1405–1416.

Chopra, A. K. (1995). *Dynamics of Structures*, volume 3. Prentice Hall New Jersey.

Corti, R., Diambra, A., Wood, D. M., Escribano, D. E., and Nash, D. F. (2016). Memory surface hardening model for granular soils under repeated loading conditions. *Journal of Engineering Mechanics*, page 04016102.

Cuéllar, P. (2011). *Pile foundations for Offshore Wind Turbines: numerical and experimental investigations on the behaviour under short-term and long-term cyclic loading.* PhD thesis, Technischen Universität Berlin.

Cuéllar, P., Mira, P., Pastor, M., Fernández-Merodo, J. A., Baeßler, M., and Rücker, W. (2014). A numerical model for the transient analysis of offshore foundations under cyclic loading. *Computers and Geotechnics*, 59:75–86.

Dafalias, Y. F. and Manzari, M. T. (2004). Simple plasticity sand model accounting for fabric change effects. *Journal of Engineering mechanics*, 130(6):622–634.

Damgaard, M., Bayat, M., Andersen, L. V., and Ibsen, L. B. (2014). Assessment of the dynamic behaviour of saturated soil subjected to cyclic loading from offshore monopile wind turbine foundations. *Computers and Geotechnics*, 61:116–126.

De Borst, R., Crisfield, M. A., Remmers, J. J., and Verhoosel, C. V. (2012). *Nonlinear finite element analysis of solids and structures.* John Wiley & Sons.

di Prisco, C. G. and Mortara, G. (2013). A multi-mechanism constitutive model for plastic adaption under cyclic loading. *International Journal for Numerical and Analytical Methods in Geomechanics*, 37:3071–3086.

di Prisco, C. G. and Wood, D. M. (2012). *Mechanical Behaviour of Soils Under Environmentally-Induced Cyclic Loads.* Springer.

Doherty, P. and Gavin, K. (2012). Laterally loaded monopile design for offshore wind farms. *Proceedings of the Institution of Civil Engineers - Energy*, 165(1):7–17.

Elgamal, A. and Lu, J. (2009). A framework for 3D finite element analysis of lateral pile system response. In *Proceedings of the International Foundation Congress and Equipment Expo. Orlando, Florida, USA*, pages 616–623. ASCE.

Elgamal, A., Lu, J., and Forcellini, D. (2009). Mitigation of liquefaction-induced lateral deformation in a sloping stratum: Three-dimensional numerical simulation. *ASCE Journal of Geotechnical and Geoenvironmental Engineering*, 135(11):1672–1682.

Elgamal, A., Yang, Z., Lai, T., Kutter, B. L., and Wilson, D. W. (2005). Dynamic response of saturated dense sand in laminated centrifuge container. *Journal of Geotechnical and Geoenvironmental Engineering*, 131(5):598–609.

Elgamal, A., Yang, Z., Parra, E., and Ragheb, A. (2003). Modeling of cyclic mobility in saturated cohesionless soils. *International Journal of Plasticity*, 19(6):883–905.

Foti, S., Lai, C. G., and Lancellotta, R. (2002). Porosity of fluid-saturated porous media from measured seismic wave velocities. *Géotechnique*, 52:359–373.

Gazzo, A., Matzen, F., Farhangi, C., and Lamdaouar, A. (2015). Offshore wind in Europe - Walking the tightrope to success. Technical report, Ernst & Young. London, UK.

Griffiths, D. V. (1985). Numerical modeling of interfaces using conventional finite elements. In *Proceedings of 5th International Conference on Numerical Methods in Geomechanics. Nagoya, Japan*, pages 837–844.

Hasselmann, K., Barnett, T. P., Bouws, E., Carlson, H., Cartwright, D. E., Enke, K., Ewing, J. A., Gienapp, H., Hasselmann, D. E., and Kruseman, P. (1973). Measurements of wind-wave growth and swell decay during the Joint North Sea Wave Project (JONSWAP). Technical report, Deutches Hydrographisches Institut. Hamburg, Germany.

Hsu, S. A., Meindl, E. A., and Gilhousen, D. B. (1994). Determining the power-law wind-profile exponent under near-neutral stability conditions at sea. *Journal of Applied Meteorology*, 33(6):757–765.

Huang, M., Yue, Z. Q., Tham, L. G., and Zienkiewicz, O. C. (2004). On the stable finite element procedures for dynamic problems of saturated porous media. *International Journal for Numerical Methods in Engineering*, 61(9):1421–1450.

Huang, N. E., Long, S. R., Tung, C. C., Yuen, Y., and Bliven, L. F. (1981). A unified two-parameter wave spectral model for a general sea state. *Journal of Fluid Mechanics*, 112:203–224.

Hughes, T. J. R. (1987). *The Finite Element Method: linear static and dynamic finite element analysis*. Prentice-Hall.

Iai, S., Morita, T., Kameoka, T., Matsunaga, Y., and Abiko, K. (1995). Response of a dense sand deposit during 1993 Kushiro-oki earthquake. *Soils and Foundations - Japanese Society of Soil Mechanics and Foundation Engineering*, 35(1):115–131.

Ishihara, K., Tatsuoka, F., and Yasuda, S. (1975). Undrained deformation and liquefaction of sand under cyclic stresses. *Soils and Foundations - Japanese Society of Soil Mechanics and Foundation Engineering*, 15(1):29–44.

Jeremić, B., Cheng, Z., Taiebat, M., and Dafalias, Y. F. (2008). Numerical simulation of fully saturated porous materials. *International Journal for Numerical and Analytical Methods in Geomechanics*, 32(13):1635–1660.

Jeremić, B., Jie, G., Preisig, M., and Tafazzoli, N. (2009). Time domain simulation of soil–foundation–structure interaction in non–uniform soils. *Earthquake Engineering and Structural Dynamics*, 38(5):699–718.

Jonkman, J. M., Butterfield, S., Musial, W., and Scott, G. (2009). Definition of a 5-MW Reference Wind Turbine for offshore system development. Technical report, National Renewable Energy Laboratory (NREL). Golden, Colorado, USA.

Journée, J. M. J. and Massie, W. W. (2000). *Offshore hydromechanics*. TU Delft.

Kallehave, D., Byrne, B. W., Thilsted, C. L., and Mikkelsen, K. K. (2015). Optimization of monopiles for offshore wind turbines. *Philosophical Transactions of the Royal Society of London A: Mathematical, Physical and Engineering Sciences*, 373(2035):1–15.

Kallehave, D., Thilsted, C. L., and Liingaard, M. (2012). Modification of the API p-y formulation of initial stiffness of sand. In *Proceedings of Offshore Site Investigation and Geotechnics: Integrated Technologies - Present and Future. London, UK*, pages 465–472. Society of Underwater Technology.

Kramer, S. L. (1996). *Geotechnical earthquake engineering*, volume 80. Prentice Hall Upper Saddle River, NJ.

Kühn, M. J. (2001). *Dynamics and design optimisation of Offshore Wind Energy Conversion systems*. PhD thesis, Delft University of Technology.

Lade, P. V. and Duncan, J. M. (1975). Elastoplastic stress-strain theory for cohesionless soil. *Journal of the Geotechnical Engineering Division*, 101(10):1037–1053.

Lanzafame, R. and Messina, M. (2007). Fluid dynamics wind turbine design: Critical analysis, optimization and application of BEM theory. *Renewable energy*, 32(14):2291–2305.

LeBlanc, C., Houlsby, G. T., and Byrne, B. W. (2010). Response of stiff piles in sand to long-term cyclic lateral loading. *Géotechnique*, 60(2):79–90.

Lombardi, D., Bhattacharya, S., and Wood, D. M. (2013). Dynamic soil–structure interaction of monopile supported wind turbines in cohesive soil. *Soil Dynamics and Earthquake Engineering*, 49:165–180.

López-Querol, S., Fernández-Merodo, J. A., Mira, P., and Pastor, M. (2008). Numerical modelling of dynamic consolidation on granular soils. *International journal for numerical and analytical methods in geomechanics*, 32(12):1431–1457.

Lu, J., Elgamal, A., and Yang, Z. (2011). *OpenSeesPL: 3D Lateral Pile-Ground Interaction*. University of California, San Diego.

Lysmer, J. and Kuhlemeyer, R. L. (1969). Finite dynamic model for infinite media. *Journal of the Engineering Mechanics Division*, 95(4):859–878.

Madsen, H. A., Bak, C., Døssing, M., Mikkelsen, R., and Øye, S. (2010). Validation and modification of the Blade Element Momentum theory based on comparisons with actuator disc simulations. *Wind Energy*, 13(4):373–389.

Manwell, J. F., McGowan, J. G., and Rogers, A. L. (2010). *Wind energy explained: theory, design and application*. John Wiley & Sons.

Masters, I., Chapman, J. C., Willis, M. R., and Orme, J. A. C. (2014). A robust Blade Element Momentum theory model for tidal stream turbines including tip and hub loss corrections. *Journal of Marine Engineering & Technology*, 10(1):25–35.

Mazzoni, S., McKenna, F., Scott, M., and Fenves, G. (2007). *OpenSees Command Language Manual*.

McGann, C. R., Arduino, P., and Mackenzie-Helnwein, P. (2012). Stabilized single-point 4-node quadrilateral element for dynamic analysis of fluid saturated porous media. *Acta Geotechnica*, 7(4):297–311.

McGann, C. R., Arduino, P., and Mackenzie-Helnwein, P. (2015). A stabilized single-point finite element formulation for three-dimensional dynamic analysis of saturated soils. *Computers and Geotechnics*, 66:126–141.

McKenna, F. T. (1997). *Object-oriented finite element programming: frameworks for analysis, algorithms and parallel computing*. PhD thesis, University of California, Berkeley.

Melendo, A., Coll, A., Pasenau, M., Escolano, E., and Monros, A. (2015). www.gidhome.com. [Online; accessed Nov-2015].

Mira, P., Pastor, M., Li, T., and Liu, X. (2003). A new stabilized enhanced strain element with equal order of interpolation for soil consolidation problems. *Computer methods in applied mechanics and engineering*, 192(37):4257–4277.

Moriarty, P. J. and Hansen, A. C. (2005). AeroDyn theory manual. Technical report, National Renewable Energy Laboratory (NREL). Golden, Colorado, USA.

Morison, J. R., O'Brien, M. P., Johnson, J. W., and Schaaf, S. A. (1950). The force exerted by surface waves on piles. *Journal of Petroleum Technology*, 2(05):149–154.

Mróz, Z., Norris, V. A., and Zienkiewicz, O. C. (1978). An anisotropic hardening model for soils and its application to cyclic loading. *International Journal for Numerical and Analytical Methods in Geomechanics*, 2:203–221.

Newman, J. N. (1977). *Marine hydrodynamics*. MIT press.

Ochi, M. K. and Hubble, E. N. (1976). Six-parameter wave spectra. *Coastal Engineering Proceedings*, 1(15):301–328.

Panofsky, H. A. and Dutton, J. A. (1984). *Atmospheric turbulence: models and methods for engineering applications*. John Wiley & Sons.

Pierson, W. J. and Moskowitz, L. (1964). A proposed spectral formulation for fully developed wind seas based on the similarity theory of S.A. Kitaigorodskii. *Journal of Geophysical Research*, 69(24):5181–5190.

Pisanò, F. and Jeremić, B. (2014). Simulating stiffness degradation and damping in soils via a simple visco-elastic–plastic model. *Soil Dynamics and Earthquake Engineering*, 63:98–109.

Preisig, M. and Prévost, J. H. (2011). Stabilization procedures in coupled poromechanics problems: A critical assessment. *International Journal for Numerical and Analytical Methods in Geomechanics*, 35(11):1207–1225.

Prévost, J. H. (1985). A simple plasticity theory for frictional cohesionless soils. *International Journal of Soil Dynamics and Earthquake Engineering*, 4(1):9–17.

Prévost, J. H. and Popescu, R. (1996). Constitutive relations for soil materials. *Electronic Journal of Geotechnical Engineering*.

Roten, D., Fäh, D., and Bonilla, L. F. (2013). High-frequency ground motion amplification during the 2011 Tohoku earthquake explained by soil dilatancy. *Geophysical Journal International*, 193(2):898–904.

Rudolph, C., Bienen, B., and Grabe, J. (2014). Effect of variation of the loading direction on the displacement accumulation of large-diameter piles under cyclic lateral loading in sand. *Canadian Geotechnical Journal*, 51(10):1196–1206.

Scott, M. H. and Fenves, G. L. (2003). A Krylov subspace accelerated Newton algorithm. In *Proceedings of 2003 ASCE Structures Congress. Seattle, Washington, USA*.

Sloan, S. W. (1987). Substepping schemes for the numerical integration of elastoplastic stress–strain relations. *International Journal for Numerical Methods in Engineering*, 24(5):893–911.

Thieken, K., Achmus, M., and Lemke, K. (2015a). Evaluation of a new p-y approach for piles in sand with arbitrary dimensions. In *Proceedings of 3rd International Symposium on Frontiers in Offshore Geotechnics. Oslo, Norway*, pages 705–710.

Thieken, K., Achmus, M., and Lemke, K. (2015b). A new static p-y approach for piles with arbitrary dimensions in sand. *Geotechnik*, 38(4):267–288.

van der Tempel, J. (2006). *Design of support structures for Offshore Wind Turbines*. PhD thesis, Technische Universiteit Delft.

van Kuik, G. A. M., Peinke, J., Nijssen, R., Lekou, D. J., Mann, J., Sørensen, J. N., Ferreira, C., van Wingerden, J. W., Schlipf, D., Gebraad, P., et al. (2016). Long-term research challenges in wind energy–a research agenda by the European Academy of Wind Energy. *Wind Energy Science*, 1:1–39.

Versteijlen, W. G., Metrikine, A. V., and van Dalen, K. N. (2016). A method for identification of an effective winkler foundation for large-diameter offshore wind turbine support structures based on in-situ measured small-strain soil response and 3D modelling. *Engineering Structures*.

Vugts, J. H., van der Tempel, J., and Schrama, E. A. (2001). Hydrodynamic loading on monotower support structures for preliminary design. In *Proceedings of Offshore Wind Energy EWEA Special Topic Conference. Brussels, Belgium*.

Watanabe, K., Pisanò, F., and Jeremić, B. (2016). Discretization effects in the finite element simulation of seismic waves in elastic and elastic-plastic media. *Engineering with Computers*, pages 1–27.

Yang, Z. and Elgamal, A. (2008). Multi-surface cyclic plasticity sand model with Lode angle effect. *Geotechnical and Geological Engineering*, 26(3):335–348.

Yang, Z., Elgamal, A., and Parra, E. (2003). Computational model for cyclic mobility and associated shear deformation. *Journal of Geotechnical and Geoenvironmental Engineering*, 129(12):1119–1127.

Zdravković, L., Taborda, D. M. G., Potts, D. M., Jardine, R. J., Sideri, M., Schroeder, F. C., Byrne, B. W., McAdam, R., Burd, H. J., Houlsby, G. T., et al. (2015). Numerical modelling of large diameter piles under lateral loading for offshore wind applications. In *Proceedings of 3rd International Symposium on Frontiers in Offshore Geotechnics. Oslo, Norway*.

Zienkiewicz, O. C., Chan, A. H. C., Pastor, M., Schrefler, B. A., and Shiomi, T. (1999). *Computational geomechanics*. Wiley Chichester.

Zienkiewicz, O. C., Chang, C. T., and Bettess, P. (1980). Drained, undrained, consolidating and dynamic behaviour assumptions in soils. *Géotechnique*, 30(4):385–395.

Zienkiewicz, O. C. and Shiomi, T. (1984). Dynamic behaviour of saturated porous media; the generalized Biot formulation and its numerical solution. *International Journal for Numerical and Analytical Methods in Geomechanics*, 8(1):71–96.

A Sensitivity of FE results to model set-up

In this Appendix, preliminary results about the setting of model size, space/time discretization and pore pressure stabilization are summarised.

A.1 Domain size

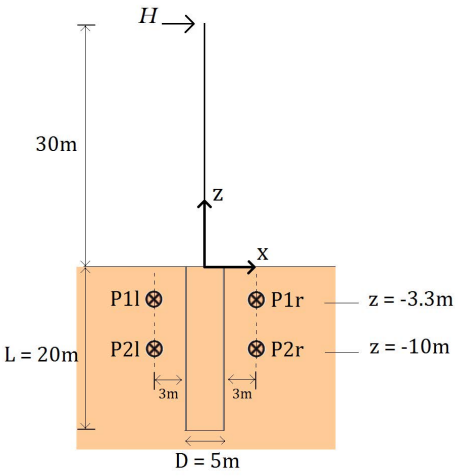

(a) geometrical specifications

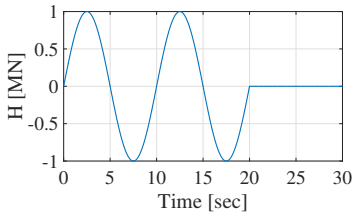

(b) load time history

Figure 17: Reference analysis case

The role played by the FE domain size is illustrated with reference to the analysis case in Figure 17. A 5 m diameter monopile is connected to a 30 m beam, loaded at the top by a sinusoidal force (frequency $f = 0.1$ Hz, amplitude $H^{max} = 1$ MN). All monopile specifications and soil parameters are as in Tables 1-2 (except soil permeability, $k = 10^{-6}$ m/s), with structure elevation equal to 30 m and no additional lumped masses. Three relatively coarse meshes, A, B and C, are first tested to explore domain size effects (Figure 18 – in all cases, the same size W is kept along the x and y directions). The corresponding FE results are reported in Figures 19–20 in terms of (i) contour plots of total displacement norm and (ii) shear stress-strain response ($\tau_{xz} - \gamma_{xz}$) at the four control points in Figure 17.

While the contour plots in Figure 19 indicate the insufficient size of mesh A (non-negligible displacements are recorded close to the outer boundaries), mesh B and C provide very similar results in terms of both displacement norm and stress-strain cycles. The size of mesh B seems thus appropriate, as well as in good agreement with the previous size settings by Cuéllar et al. (2014).

A.2 Space/time discretization

The sensitivity to space discretization is investigated starting from the above mesh B, then renamed B1 and further refined. The gradual mesh refinement is illustrated in Figure 21 for the three meshes B1, B2, B3, formed by approximately 3000, 6000 and 8000 ssp elements. The analysis case in Figure 17 is numerically studied in combination with the three meshes above, and the corresponding results plotted in Figure 22 (contour plots of excess pore pressure Δu) and Figure 23 ($\tau_{xz} - \gamma_{xz}$ cycles at the four control points in Figure 17).

In this case, the influence on the excess pore pressure field does not seem dramatic, while substantial mesh effects are visible in the shear stress-strain response at points P1l and P1r. The

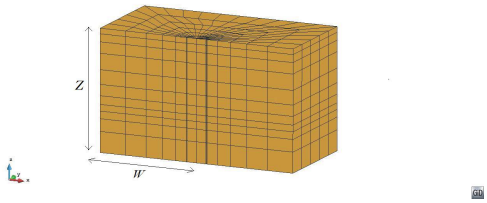

(a) Mesh A: $Z = 30\,\mathrm{m}$, $W = 25\,\mathrm{m}$

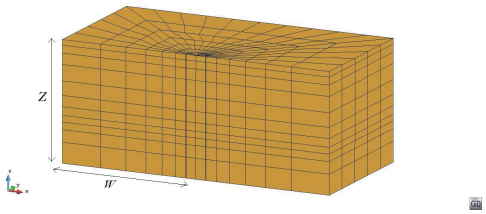

(b) Mesh B: $Z = 30\,\mathrm{m}$, $W = 35\,\mathrm{m}$

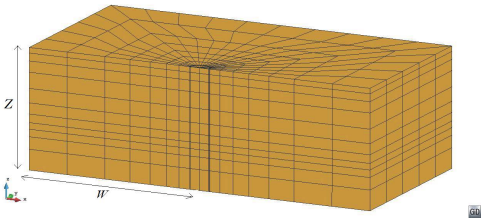

(c) Mesh C: $Z = 30\,\mathrm{m}$, $W = 45\,\mathrm{m}$

Figure 18: FE meshes employed for domain size sensitivity analysis

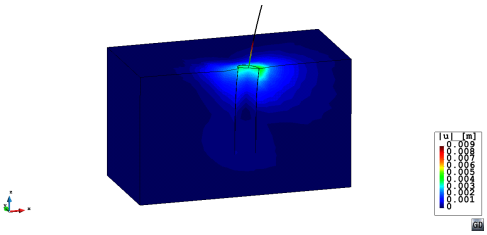

(a) Mesh A

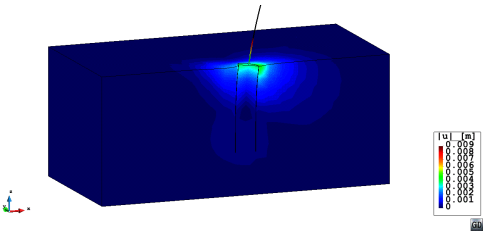

(b) Mesh B

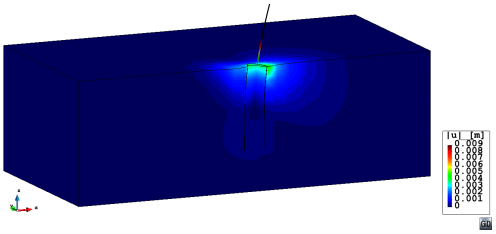

(c) Mesh C

Figure 19: Domain size sensitivity analysis: total displacement norm at the second positive load peak (Figure 4b)

medium mesh B2 seems a reasonable compromise between accuracy and computational costs – the latter significantly increase for mesh B3. Further, mesh B2 compares well with the space discretization set by Cuéllar et al. (2014) for a similar OWT problem. Both in Cuéllar et al. (2014) and this study, the seeming coarseness of the adopted meshes is substantially remedied by the use of 8-node elements based on enhanced assumed strain formulations (Mira et al., 2003; McGann et al., 2015).

As for time marching, the time-step size $\Delta t = 0.004$ s reported in Section 3.4 is 1/10 of the sampling step size in the anemometric records, and fulfils the requirement $\Delta t < \Delta x_{avg}/V_s$ with $\Delta x_{avg} \approx 1$ m and $\Delta V_s \approx 200$ m/s. Further, Krylov-Newton step iterations (Scott and Fenves, 2003) are arrested when an error criterion on the incremental displacement norm is satisfied with relative tolerance equal to 7.5×10^{-4} (Mazzoni et al., 2007). Although smaller time-steps may suit better the integration of highly non-linear soil models (Jeremić et al., 2009; Watanabe et al., 2016), the selection of Δt (and of the error tolerance) is largely driven by computational cost

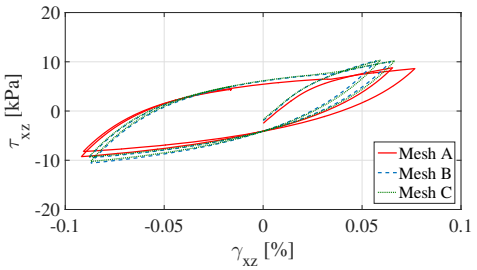

(a) Control point P1l

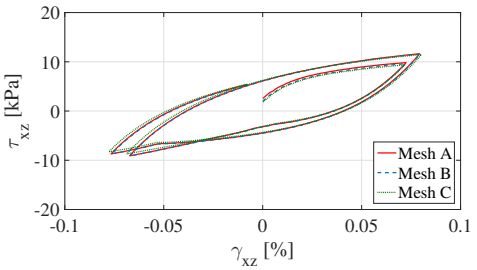

(b) Control point P1r

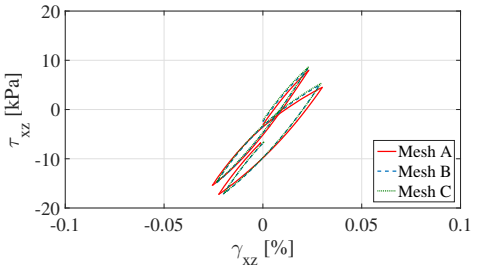

(c) Control point P2l

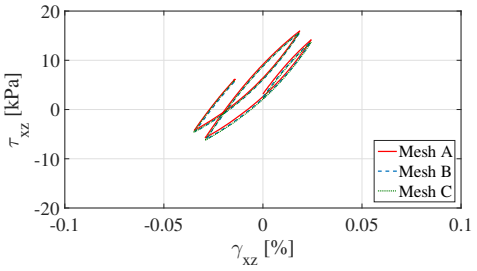

(d) Control point P2r

Figure 20: Domain size sensitivity analysis: $\tau_{xz} - \gamma_{xz}$ cycles at the four control points in Figure 17b

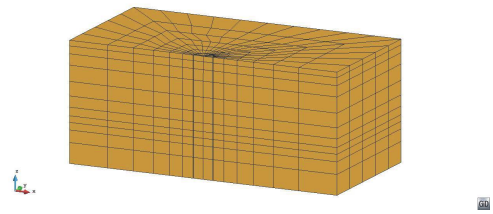

(a) Mesh $B1$ (coarse)

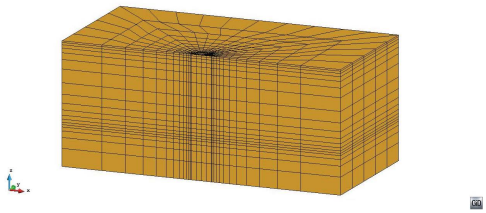

(b) Mesh $B2$ (medium)

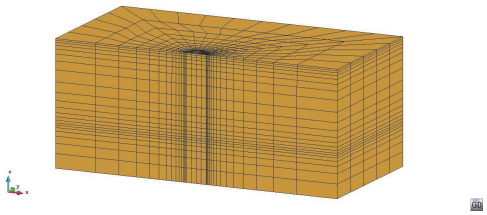

(c) Mesh $B3$ (fine)

Figure 21: FE meshes employed for mesh sensitivity analysis

arguments.

A.3 Pore pressure stabilisation

The effect of the stabilization parameter α in Equation (2) is illustrated in Figure 24 for the same analysis case in Figure 17. The excess pore pressure contour plots at the first positive load peak (Figure 17b) are reported for the following four cases, all analysed through the coarse mesh A (Figure 18a) for computational convenience: (i) H1-P1ssp elements with inhibited stabilization ($\alpha = 0$); (ii) H1-P1ssp elements stabilised with a low α value ($\alpha = 10^{-7}$); (iii) H1-P1ssp elements and $\alpha = 10^{-5}$ (from Equation (3)); (iv) standard H1-P1 elements (no stabilisation).

Checkerboard pressure patterns are apparent in Figures 24a and 24d (no stabilisation) and,

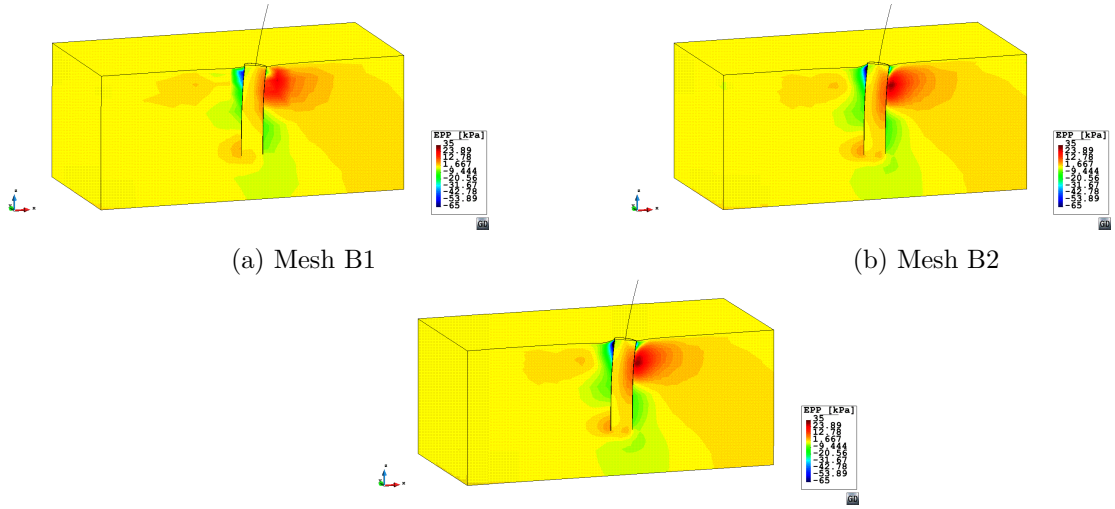

(a) Mesh B1

(b) Mesh B2

(c) Mesh B3

Figure 22: Mesh sensitivity analysis: excess pore pressure at the second positive load peak (Figure 4b)

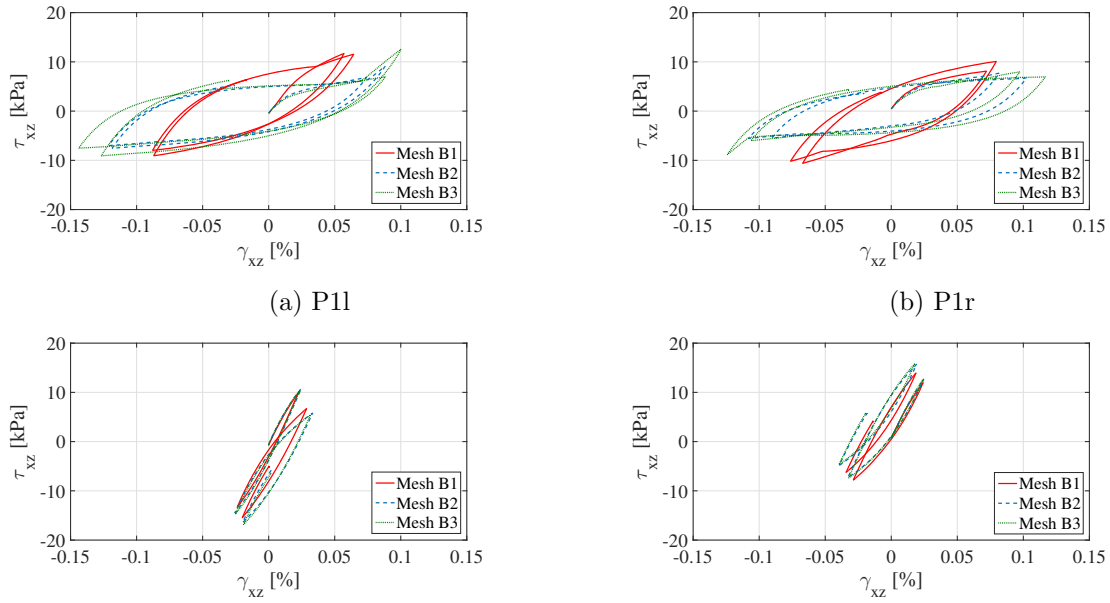

(a) P1l

(b) P1r

(c) P2l

(d) P2r

Figure 23: Mesh sensitivity analysis: $\tau_{xz} - \gamma_{xz}$ cycles at the four control points in Figure 17

to a lesser extent, in Figure 24b as well, where $\alpha = 10^{-7}$ proves still too low for satisfactory stabilisation. Conversely, a smooth pore pressure field results when $\alpha = 10^{-5}$ is calibrated through Equation (3) (Figure 24c), with pressure amplitudes overall comparable to the other unsatisfactory cases. The final value $\alpha = 6 \times 10^{-6} < 10^{-5}$ used in the main simulations (Section 3.4) has been determined to comply with Equation (3) in presence of the finer mesh B2 (Figure 21b).

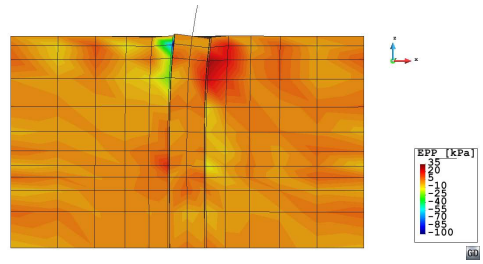

(a) H1-P1ssp: $\alpha = 0$

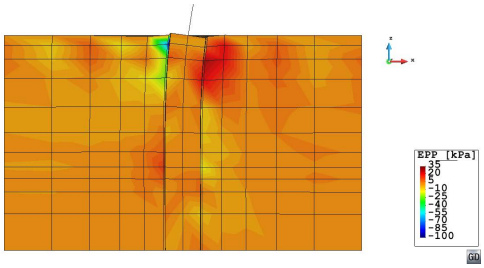

(b) H1-P1ssp: $\alpha = 10^{-7}$

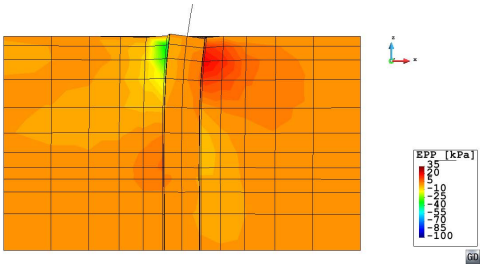

(c) H1-P1ssp: $\alpha = 10^{-5}$

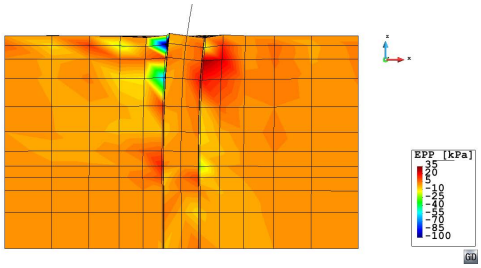

(d) H1-P1

Figure 24: Pressure stabilization analysis: excess pore pressure at the first positive load peak (Figure 4b)